



LAWRENCE
LIVERMORE
NATIONAL
LABORATORY

High resolution simulations of ignition capsule designs for the National Ignition Facility

D. S. Clark, S. W. Haan, A. W. Cook, M. J. Edwards, B. A. Hammel, J. M. Koning, M. M. Marinak

March 24, 2011

Physics of Plasmas

Disclaimer

This document was prepared as an account of work sponsored by an agency of the United States government. Neither the United States government nor Lawrence Livermore National Security, LLC, nor any of their employees makes any warranty, expressed or implied, or assumes any legal liability or responsibility for the accuracy, completeness, or usefulness of any information, apparatus, product, or process disclosed, or represents that its use would not infringe privately owned rights. Reference herein to any specific commercial product, process, or service by trade name, trademark, manufacturer, or otherwise does not necessarily constitute or imply its endorsement, recommendation, or favoring by the United States government or Lawrence Livermore National Security, LLC. The views and opinions of authors expressed herein do not necessarily state or reflect those of the United States government or Lawrence Livermore National Security, LLC, and shall not be used for advertising or product endorsement purposes.

High resolution simulations of ignition capsule designs for the National Ignition Facility

D. S. Clark, S. W. Haan, A. W. Cook, M. J. Edwards, B. A. Hammel, J. M. Koning,
and M. M. Marinak

Lawrence Livermore National Laboratory
Livermore, CA 94550

This work was performed under the auspices of the U.S. Department of Energy by Lawrence Livermore
National Laboratory under Contract DE-AC52-07NA27344.

Abstract

Ignition capsule designs for the National Ignition Facility (NIF) [G. H. Miller, E. I. Moses, and C. R. Wuest, *Opt. Eng.* **443**, 2841 (2004)] have continued to evolve in light of improved physical data inputs, improving simulation techniques, and—most recently—experimental data from a growing number of NIF sub-ignition experiments. This paper summarizes a number of recent changes to the cryogenic capsule design and some of our latest techniques in simulating its performance. Specifically, recent experimental results indicated harder x-ray drive spectra in NIF hohlraums than were predicted and used in previous capsule optimization studies. To accommodate this harder drive spectrum, a series of high-resolution 2-D simulations, resolving Legendre mode numbers as high as two thousand, were run and the germanium dopant concentration and ablator shell thicknesses re-optimized accordingly. Simultaneously, the possibility of cooperative or nonlinear interaction between neighboring ablator surface defects has motivated a series of fully 3-D simulations run with the massively parallel HYDRA code. These last simulations include perturbations seeded on all capsule interfaces and can use actual measured shell surfaces as initial conditions. 3-D simulations resolving Legendre modes up to two hundred on large capsule sectors have run through ignition and burn, and higher resolution simulations resolving as high as mode twelve hundred have been run to benchmark high-resolution 2-D runs. Finally, highly resolved 3-D simulations have also been run of the jet-type perturbation caused by the fill tube fitted to the capsule. These 3-D simulations compare well with the more typical 2-D simulations used in assessing the fill tube's impact on ignition. Coupled with the latest experimental inputs from NIF, our improving simulation capability yields a fuller and more accurate picture of NIF ignition capsule performance.

I. Introduction

Experiments have begun on the National Ignition Facility (NIF) [1] with the goal of achieving indirect drive inertial confinement fusion (ICF) ignition [2] as part of the National Ignition Campaign (NIC) [3]. Since August of 2009, a number of laser shots have been performed on NIF to test several of the key sub-goals that must be accomplished to make feasible an integrated ignition attempt [4]. These include achieving adequate hohlraum radiation temperatures at tolerable levels of laser backscatter and achieving adequate low mode implosion symmetry, among others [5]. Other critical components that are now being tested include the tuning of the radiation pulse so as to sequence correctly the passage of the accelerating shocks through the deuterium-tritium (DT) fuel [6] and the technological challenge of experimentally fielding adequately symmetric and smooth DT fuel layers to enable suitably symmetric implosions. The requirements [12] for each of these ignition sub-goals (radiation temperature, symmetry, layer smoothness, etc.) have been guided both by extensive experimental campaigns on previous facilities and by an intensive simulation effort using sophisticated radiation hydrodynamics codes. In turn, the results of the past year's NIF experiments have fed back on the simulation effort both to modify how simulations are run (and so improve agreement with the experimental data) and to suggest modifications to the ignition target design [13].

One feature of the ignition target design that has already been modified in accordance with the first round of NIF experiments is the concentration and distribution of germanium (Ge) dopant added to the plastic (CH) ablator shell. The role of the Ge dopant is to attenuate the flux of hard x-ray radiation through the ablator shell and thereby prevent pre-heating of the DT fuel and inner ablator layers. In addition to increasing the entropy of the fuel and therefore reducing its compressibility, pre-heating of the neighboring DT and CH layers has the important effect of changing the relative densities and hence Atwood number at the fuel-ablator interface. The Atwood number at this interface in turn

strongly influences the susceptibility of the interface to the Richtmyer-Meshkov (RM) and Rayleigh-Taylor (RT) instabilities and hence mix of high-Z ablator material into the DT fuel [11]. As such, for a given hard x-ray fraction incident on the ignition capsule, adjusting the Ge concentration provides a strong lever for controlling the stability of the fuel-ablator interface. High-resolution radiation hydrodynamics simulations have been used to re-optimize this dopant concentration in the light of the 2009 NIF experimental data base.

Accurately simulating the stability of the fuel-ablator interface is particularly pressing given that it is difficult to diagnose experimentally the degree of instability or material mixing that is occurring at this interface in an actual implosion. Nevertheless, experimental techniques for diagnosing high-mode mix are being developed [7]. The difficulty of performing such measurements reflects primarily that the process to be diagnosed occurs over extremely small spatial and temporal scales as well as deep within the imploding capsule where diagnostic signatures can be easily obscured. Likewise, because of the wide range of relevant scales involved, accurately simulating the behavior of the fuel-ablator interface is a challenging undertaking in its own right.

Another challenge in improving the resolution and fidelity of capsule simulations is accurately representing the dimensionality of capsule perturbations. So long as perturbations to the imploding capsule remain small, it is well known that the growth of such perturbations does not distinguish between two-dimensional (2-D) and three-dimensional (3-D) features [8]. Because of this 2-D/3-D equivalence, and because of the computational demands of 3-D, capsule instability simulations are mostly run in 2-D. The actual 3-D character of the surface can then be reconstructed either by summing individual modes in Fourier space or by enhancing the surface roughness initialized in the simulation so as to capture an effective 3-D roughness in 2-D. However, as perturbations grow into the nonlinear regime, the subsequent 2-D and 3-D developments will differ, and, specifically, the

perturbation growth in 3-D can be expected to be faster than in 2-D [9]. Nonlinearity, albeit weakly, is especially anticipated for the very high mode numbers present at the fuel-ablator interface, and the 2-D/3-D dichotomy can be expected to be most pronounced there. To simulate accurately the mixing at this interface, fully 3-D simulations are then necessary.

Yet another area where 2-D and 3-D instability development can be expected to differ is in the growth of isolated surface defects. The preeminent example of these types of perturbations is the glass fill tube attached to the capsule in order to fill the capsule shell with its DT fuel. In this case, simulations indicate that the fill tube launches a jet of glass mixed with ablator material through the DT fuel layer as the shell is imploding [10,11]. Highly elongated features, such as this fill tube-induced jet, can be expected to behave differently in 3-D than in 2-D. In particular, the highly elongated jet might be anticipated to break up in 3-D, and hence be less penetrating. Again, since the simulations used to quantify this effect have been exclusively run in 2-D, a comparison to fully 3-D simulations is warranted.

The purpose of this paper is to summarize the high-resolution radiation hydrodynamics simulations used in re-optimizing the ignition capsule design following the first round of NIF experiments as well as the smaller set of 3-D simulations used to benchmark the larger data set of 2-D simulations. This paper is organized as follows. Sec. II briefly summarizes the salient features of the NIF ignition capsule design, as described in detail elsewhere [12], along with the recent NIF experimental data that bears on high-mode mix. Sec. III then describes 2-D simulations directed at assessing fuel-ablator mix in the NIF ignition design and culminating in an optimized dopant distribution for that design. Sec. IV extends these results from 2-D into 3-D as a verification of the results of Sec. III. A lower resolution 3-D simulation which spans a larger sector of the capsule and

was run through ignition and burn is also described. Sec. V further compares 2-D to 3-D results but in the context of the fill tube-induced jet. Finally, Sec. VI concludes.

II. NIF ignition capsule design and recent experiments

The latest revision of the NIF ignition capsule design, designated “Rev. 5,” has recently been described in Ref. [12] and is illustrated in Fig. 1. Similar to previous designs, Rev. 5 uses a plastic (CH) ablator doped with germanium in a narrow sequence of layers close to the inside of the plastic shell. A layer of DT fuel is frozen on the inside of the ablator shell to a thickness of 68 μm . Compared to the preceding “Rev. 4” design [13], the current design has a smaller outer radius (and hence uses less laser energy, 1.3 MJ compared to 1.55 MJ, to be driven at the same 300 eV radiation temperature), has a proportionately thicker ablator shell and fuel layer, for increased stability, and has a higher dopant concentration (1.0 at. % maximum concentration compared to the previous 0.5 at. %). Reducing the capsule radial scale reduces the design’s margin to failure but, of course, reduces the demands on the laser system to deliver the required energy. Increasing the shell thickness and dopant concentration can increase the design’s hydrodynamic stability but naturally come at the cost of reducing its implosion velocity. For a fixed amplitude of perturbations around the igniting hot spot (resulting from RM and RT instability growth), this reduced implosion velocity increases the chance of ignition failure. The designed implosion velocity for Rev. 4 was 384 km/s, while for Rev. 5 it has been reduced to 370 km/s. Hence, in general terms, the design modifications made in evolving from Rev. 4 to Rev. 5 have traded 1-D performance, in the sense of lower implosion velocity, for increased stability with respect to 2-D/3-D hydrodynamic instabilities. These general considerations of hydrodynamic stability and 1-D ignition probability inform the choices made in reaching a final

design. To reach the specific target design with dopant concentrations and layer thickness as shown in Fig. 1, however, requires the detailed simulations discussed below.

Outside of the reduction in capsule scale and energy, the changes made to the capsule design in evolving from Rev. 4 to Rev. 5 are a direct consequence of the results of the 2009 NIF experimental campaign. With regard to capsule design, one of the most important observations from the 2009 campaign was the dependence of the hard x-ray component of the hohlraum radiation spectrum on hohlraum radiation temperature [14] as summarized in Fig. 2. Here, hard x-ray component refers to the fraction of x-ray energy incident on the capsule with photon energy greater than 1.8 keV and is associated with gold M-band emission. In the figure, each of the diamonds represents a simultaneous measurement of the hard x-ray fraction and the internal hohlraum radiation temperature from a NIF hohlraum experiment. The squares and circles, respectively, represent simulations of each of these experiments run with the HYDRA [15] and Lasnex [16] radiation hydrodynamics codes. It is clear from the figure that the hard x-ray fraction at a given hohlraum drive temperature is consistently underestimated by the simulations and especially so in the Lasnex simulations. Both the Lasnex and HYDRA simulations used the XSN opacity model [17, 18], and the Lasnex simulations used coarser zoning in the hohlraum wall than is now considered appropriate. Since this ensemble of simulations was run, a hohlraum model has been developed using the DCA atomic physics model [19]. This model provides a good fit to many experimental observables [14]; however, the hard x-ray fraction predicted from this revised model is now somewhat higher than seen in experiments.

Also shown in the figure are curves representing hard x-ray fraction as a function of radiation temperature taken from representative x-ray sources used to drive high-resolution, capsule-only simulations; these curves may be thought of as parametric in time with the radiation drive temperature increasing over the course of the implosion. The solid curve represents a source taken from a Lasnex

hohlraum simulation which is consistent with the Lasnex hohlraum simulations at peak flux; the dashed curve represents a source taken from a HYDRA hohlraum simulation; and finally the dash-dot curve represents the HYDRA source but with the hard x-ray fraction multiplied by a factor of 1.2. Since the dash-dot curve shows good consistency with the data base of measured NIF hard x-ray fraction, the Rev. 5 capsule design was re-optimized using this revised x-ray source. Note that the apparent hard x-ray fraction at the peak drive temperature of 300 eV has increased from approximately 13 % (essentially the Planckian value) to nearly 18 % with the revised source.

Given that the previous Rev. 4 design was optimized using an x-ray source similar to that shown by the solid line [13], it is unsurprising that some revision to the design was necessary. This is emphasized by the results shown in Fig. 3. The figure compares snapshots of the density profiles during the acceleration phase for the current Rev. 5 design and for the previous Rev. 4 design but driven with the updated hard x-ray fraction. The notch adjacent to the maximum in each profile marks the location of the unstable interface between the cold DT fuel to the left and the hotter CH ablator to the right. With the updated hard x-ray fraction, the previous Rev. 4 design has a clearly larger Atwood number at the fuel-ablator interface when compare to Rev. 5 and can be expected to have more mixing at this interface. The quantitative (and dramatic) increase in mix with this increased Atwood number is shown by comparing Figs. 5 and 6 below. First, however, the following section summarizes the simulation method used in assessing high-mode fuel-ablator mix.

III. 2-D high-mode simulations

High-resolution 2-D simulations run with HYDRA have been the platform used in re-optimizing the Rev. 5 capsule design with respect to fuel-ablator mix. Similar simulations have been used in optimizing previous beryllium ablator designs [11] and in assessing the impact of the capsule fill tube

[10]. These simulations are typically run on 15° “wedges” at the “waist” of the capsule with zoning sufficient to resolve perturbations at Legendre mode numbers up to $\ell = 1,200$, that is, typically one thousand zones in both the radial and angular directions. The zoning scheme is also chosen so that no zone has an angular-to-radial aspect ratio greater than twelve-to-one or less than one-to-two in the shell. Since the wedge extends over only 15° , the lowest mode number resolved in the simulation is $\ell = 12$; larger wedges can, of course, be simulated but are more costly in computation time for the same resolution and are not expected to alter the results significantly. The simulations are run at the capsule waist since the reflecting boundary condition is most accurate there and since this avoids the complexities of combined 2-D/3-D effects that occur near the capsule pole.

A typical simulation will use perturbations initialized on all of the capsule interfaces: the inside and outside ablator surfaces, the inner ice surface, and all of the internal surfaces between the differently doped layers. The perturbation amplitudes for each individual layer are taken from roughness power spectra which derive from a fit to measured shell surface roughnesses as well as feedback from simulations. The power spectra used in the simulations of Rev. 5 are shown in Fig. 4. Each of these represents the maximum allowed power according to the requirements for ignition [12]. A random sign is applied to each modal amplitude to account for the random phasing of modes. Finally, the perturbations are introduced into the mesh by warping the mesh lines at the given interface according to the power spectrum roughness for each mode number, and then “feathering” away the mesh perturbation radially away from the perturbed interface according to the linear Legendre *eigen* function for that mode, that is, r^ℓ or $r^{-\ell-1}$ with r the radial coordinate. This so-called “Legendre feathering” gives the most accurate representation of the (predominately) linear evolution of each individual mode.

Fig. 5 shows the result of a simulation of the current Rev. 5 design resolving modes $\ell = 12 - 1,200$. The snapshot shows the material region on the left and density on the right at the time of peak implosion velocity (20.98 ns). The short wavelength penetration of the ablator dopant layers (green and light blue) into the DT fuel (dark blue) is evident. Note that the relatively low mode features ($\ell \cong 30$) grow coherently at the ablation front (visible at the top of the figure) and at the fuel-ablator interface.

A figure of merit useful in comparing the relative amount of mix between simulations of different designs is the fuel clean mass fraction. This quantity is also used to parameterize the impact of fuel-ablator in the margin formalism described in Ref. [12]. This fraction is defined as the fraction of the initial DT fuel mass contaminated by 5 % or less by mass of ablator material at peak velocity. From the simulation shown in Fig. 5, the Rev. 5 2-D clean mass fraction for modes 12 – 1,200 is 0.77. Based on repeated simulations using different random number seeds to initialize the capsule surface roughness, the clean mass fraction has a variability at the level of a few percent. Also, as a test of convergence, simulations have been run with resolution up to $\ell = 2,400$. Although finer scale features appear in these simulations compared to the standard resolution, the clean fraction decreases by only a few percent at this resolution. On the other hand, decreasing the resolution to include only up to $\ell = 600$ gives a higher clean fraction by 5 to 10 % compared to $\ell = 1,200$. On these grounds, a resolution of $\ell = 1,200$ is deemed to be converged for the designs of interest. It should also be borne in mind that, at scales corresponding to mode numbers $\ell \geq 1,200$, the additional physics of viscosity and molecular diffusion are expected to play a role. As these effects are not currently included in HYDRA, simulations in this mode range are a questionable addition to the understanding of fuel-ablator mix.

The difference in the 1-D density profiles between Rev. 5 and Rev. 4 in light of the increased hard x-ray fraction was shown in Fig. 3. The effect on the 2-D mixing at the fuel-ablator interface can be seen by comparing Fig. 5 to 6. The latter figure is the analogue to Fig. 5, using the same roughness seeds and source spectrum, but with the Rev. 4 dopant levels and dimensions. The higher fuel-ablator Atwood number accompanying the lower dopant level results in extreme, near-turbulent mixing of the ablator into the fuel layer at peak velocity. Tendrils of high-Z ablator have penetrated nearly completely through the fuel and substantial secondary Kelvin-Helmholtz vortices are apparent. The fuel clean fraction computed from this simulation is only 0.21. Rev. 5, with its clean fraction of 0.77, is a clearly more optimal design given the x-ray spectra measured in NIF hohlraums.

Figs. 5 and 6 represent polar extremes of tolerable and intolerable high-mode mix. To reach the optimum represented by the final Rev. 5 design, a series of high-resolution simulations of the type just described was run. The data base of these simulations is summarized by Fig. 7 in a plot of clean mass fraction versus ablator dopant concentration. The open symbols represent simulations run at the previous 1.55 MJ scale of Rev. 4, and the filled symbols represent the reduced Rev. 5 scale of 1.3 MJ. The leftmost point in the figure represents the previous Rev. 4 design with its 0.5 at. % dopant concentration and (with the updated hard x-ray fraction) clean mass fraction of 0.21. Increasing the peak dopant concentration in this design to 0.8 at. % improves the fuel-ablator Atwood number in this design and with it the clean fraction increases to 0.57. The error bars on this point represent the uncertainty in the amount of dopant in fabricated shells (0.01 at. % due to uncertainties in shell metrology), and the effect on the clean fraction of the anticipated 10 % uncertainty in the measured hard x-ray fraction. Interestingly, the fabrication and hard x-ray fraction uncertainties both result in an approximately 10 % uncertainty in fuel clean fraction.

Maintaining the 0.8 at. % dopant concentration but now reducing the scale to 1.3 MJ only slightly reduces the clean mass fraction to from 0.57 to 0.55. By increasing the dopant from 0.8 to 1.0 at. %, the clean fraction can be increased to 0.72. As represented by the filled squares and diamond, thickening both the DT fuel and the plastic ablator by 5 μm , respectively, further increases the clean fraction to 0.77. Interestingly, increasing the dopant concentration further to 1.2 at. % causes the clean fraction to decrease. This decrease results from the effect that, while increasing the dopant concentration further stabilizes the Atwood number at the fuel-ablator interface, it also increases the density gradient at the ablation front since it is the doped ablator material that is being ablated near the time of peak velocity. At high enough concentrations, this steepened ablation front and associated instability become the dominant contributor to perturbations at the fuel-ablator interface, and the clean fraction eventually decreases with increasing concentration. As emphasized by the fitting curve drawn through the data points, a maximum in clean mass fraction then occurs at ~ 1.0 at. % dopant. The diamond at a clean fraction of 0.77, with a thick ablator and fuel layer, thus represents the final, optimal Rev. 5 design.

Note that, in all of these simulations, the dopant layer thickness was scaled in such a way as to maintain nearly constant implosion velocity as the dopant concentration is increased. Empirically, it has been shown that scaling the width of the dopant layer as the inverse square root of the dopant concentration approximately preserves the implosion velocity [20]. In this way, by maintaining a constant implosion velocity with increasing dopant, the 1-D ignition margin should not be compromised even as the 2-D/3-D stability is being improved.

The simulations summarized in Fig. 7 were initialized with all of the sources of roughness expected in experiment, *i.e.*, roughness applied to all of the internal and external capsule interfaces. To understand the relative contributions of each interface to the overall clean fraction, however, it is

useful to rerun the optimized Rev. 5 simulation with only the individual sources of roughness. Fig. 8 shows a tableau of simulations of Rev. 5 but with initial roughness applied only to the inner ice surface, the fuel-ablator interface, the internal dopant layers, and the ablator surface, respectively. While the ice surface is initially the roughest surface in the simulation, it apparently contributes little to the final fuel mix fraction. From the simulation with ice roughness only (a), the clean fraction is 0.96, *i.e.*, only 4 % mix results from the ice. A similar result derives from initializing roughness at only the fuel-ablator interface (b); in this case, the clean fraction is 0.93. It is also interesting to observe from (b) that, even though the roughness is applied to the fuel-ablator interface (the interface between the dark and light blue regions in the color map), the largest amplitude growth occurs at the boundary adjacent to the fuel-ablator interface, namely, the interface between the undoped ablator and first doped region (light blue to light green in the color map). This is a consequence of the fact that, at this high dopant concentration, the Atwood number between the fuel and undoped ablator is actually lower (and therefore more stable) than the Atwood number between the undoped ablator and first doped layer (see Fig. 3). Though this Atwood number causes larger amplitude growth at this interface, the standoff between this layer and the fuel-ablator interface of interest is sufficient to attenuate this perturbation and actually give the optimal (minimum) amount of fuel-ablator mix. Interestingly, directly seeding the perturbations at the internal dopant layers, as in (c), does not show as much growth at these internal interfaces as does seeding the fuel-ablator interface, even though the seeded amplitude is larger at the internal interfaces than at the fuel-ablator interface. The mix fraction in this case is a mere 0.01. The differences in growth seen in Figs. (b) and (c) can only be ascribed to subtleties of the time-dependent Atwood number at the fuel-ablator interface and its effect on the RM phase growth of the various shocks transiting the ablator.

Finally, initializing roughness only on the outer ablator surface, as shown in (d), shows that the relatively low mode ($\ell \cong 30$) perturbations that dominate the ablation front feed through and contribute substantially to the fuel-ablator mix. The mix fraction from ablator surface roughness alone amounts to 0.16. Of the three roughness sources considered, this then is the largest contributor to the 0.23 mix fraction when all sources are combined. Note, however, that the RMS sum of the mix fractions from Figs. (a) – (b) sums to 0.18, *i.e.*, less than the mix fraction of 0.23 when all sources are included at once. Clearly, a nonlinear interaction of the various seeds of mix causes an increase in the mix fraction when all sources are present. This effect can be identified by a close inspection of Fig. 5. Fig 5 has, at the fuel-ablator interface, a superposition of the low-mode ablator perturbations as well as high-mode tendrils of ablator poking into the fuel. Fig. 8(b) shows something like these tendrils growing at the internal dopant layers, but not at the fuel-ablator interface; and hence the mix fraction in (b) amounts to only 0.07. On the other hand, when all of the sources are coupled together, the short wavelength growth, initially growing at the internal dopant layers, is able to couple through to the fuel-ablator interface and increases the total mix fraction compared to each source in isolation. This coupling is facilitated by the ablation front growth whose larger amplitude, longer wavelength perturbations thin the undoped CH layer between the fuel and the doped CH and thereby reduces the standoff between the internal dopant interfaces and the fuel-ablator interface sufficient for the short wavelength modes to couple through. That the tips of the long wavelength perturbations feature a number of small, short-wavelength fingers of ablator pointing into the fuel underscores this effect.

IV. 3-D simulations

Fuel-ablator interface perturbations of the like shown in Figs. 5 and 6 have reached the threshold of weak nonlinearity. This is indicated by the amplitude to wavelength ratio being much greater than

unity at the finest scales visible in the figure. In the weakly nonlinear regime, it is expected that the development of RT instabilities differs in two versus three dimensions [9], namely that the bubbles of ablator material that rise into the denser fuel (that is, the downward direction in Fig. 5) travel faster in 3-D than they do in 2-D. A faster bubble rise rate than simulated in Fig. 5 would mix more ablator material into the fuel and would be expected to decrease the clean fuel fraction. Of course, the 3-D development will pertain in any actual experiment, and it is therefore necessary to benchmark the 2-D results presented in Figs. 5 – 8 against 3-D simulations.

The result of a 3-D simulation of high-mode growth in Rev. 5, analogous to the 2-D simulation of Fig. 6, is shown in Fig. 9. The rendering shows the mixing at the fuel-ablator interface at peak velocity with the color scale giving the density. Given the significantly higher computational demands of running simulations in 3-D, this simulation includes only a wedge of $2.5^\circ \times 2.5^\circ$ at the capsule waist with $1,006 \times 256 \times 256$ zones in the radial and angular directions, respectively. This should be compared with the 15° wedge using $1,217 \times 1024$ zones from Fig. 5. Otherwise, the simulation includes the 3-D analogue of the roughness initialized in Fig. 5, including all Legendre modes in the range $\ell = 72 - 1,200$ and all of their corresponding azimuthal m -modes.

The inset in the figure zooms in on the mixing layer between the dense fuel (predominantly red in the color scale) and the less dense (yellow to green) plastic ablator. As in the 2-D case, tendrils of ablator material are visible reaching five to ten microns into the fuel from the perturbed fuel-ablator interface. For comparison, the compressed fuel layer is approximately twenty microns thick at this time. Secondary Kelvin-Helmholtz (KH) instabilities can also be seen developing at the tips of the bubbles of ablator material. Note that this is contrary to the typical development of nonlinear RT mixing at this Atwood number for which the KH vortices develop at the spike tips and not at the bubble heads. This interesting feature of the mix layer is even more apparent in Fig. 10. This figure

shows a rendering of the fuel-ablator interface at the same time as Fig. 9 viewed from the fuel side of the interface (a) and also from the ablator side (b). The penetrating bubbles of less-dense ablator material (as seen from the fuel side of the interface) are all capped with developing mushroom heads, while the spike sheets of dense fuel falling into the lower density ablator (as seen from the ablator side) remain sharp and without secondary vortex development. This difference could result from the different density gradients that the bubble and spike flows penetrate. Alternately, the lower rate of shear about the more 2-D spike sheets as compared to the more 3-D bubble heads could be responsible in the unique appearance of KH vortices at the bubble side of the mix layer as opposed to the more typical spike side. Whether this phenomena is more universal or limited to the particular case of this target design is an interesting topic for further investigation.

Overall, the mix layer appears more developed (with longer tendrils and larger bulk perturbations) in the 3-D simulation than in the 2-D analogue; this is as expected. Interestingly, however, computing the clean mass fraction from the 3-D gives a value of 0.76 which is surprisingly close to the 2-D value of 0.77. Note, though, that due to the smaller angular extent of the 3-D simulation, the lowest Legendre mode that can be included is $\ell = 72$. As illustrated by Fig. 8, the 3-D simulation then omits the important contribution of lower mode ablation front growth ($\ell \cong 30$) to the fuel mix fraction. Had these modes been included in the simulation of Fig. 9, the fuel mix fraction could be expected to be higher than given by this simulation. Including $\ell \cong 30$ in a 3-D simulation increases the computational demands by roughly four fold and remains a subject of future work. Nevertheless, though the mix fraction including all Legendre modes might be higher than suggested by Fig. 9, the most important conclusion to be drawn from Fig. 9 is that the mixing layer, while nonlinear, remains coherent and not turbulent. If the instability development in 3-D were found to be turbulent, the connection between 3-D reality and the 2-D data base summarized in Fig. 7, and used to optimize the ablator dopant

concentration, would be a tenuous one. Since the mixing layer remains coherent, however, the translation from the 2-D data base to 3-D reality represents a change in the degree of mixing but not a fundamental change in the character of the mixing process. Likewise, the optimum dopant concentration that minimizes the mix in 2-D can then be taken as a good approximation to the value that minimizes the mix in 3-D. Future 3-D simulations over larger domains will aim to verify this.

Beyond the very high-mode fuel-ablator perturbations that have been discussed in this and the preceding sections, a comparison of 2-D and 3-D simulations is desirable in the lower mode range as well ($\ell \leq 200$). The reason for this is that, while lower mode perturbations have generally lower growth rates and are therefore less likely to reach the nonlinear stage of growth, it is nonetheless possible that the initial perturbation amplitudes at these lower mode numbers could be sufficiently large that, despite a slower growth rate, they still reach the threshold of nonlinearity. At that nonlinear stage, the 2-D development (as captured in most simulations) will again be different than the 3-D development that occurs in reality. This is particularly of interest since it is known that fabricated shells possess a number of isolated defects corresponding to the mode range of $\ell \sim 100$ which can be quite large. Typically, these defects are characterized as dome-shaped bumps or divots on the ablator surface with widths of order $10\ \mu\text{m}$ and heights up to several hundred nanometers. Note that nonlinearly large but rotationally symmetric perturbations can be accurately simulated in 2-D by placing the perturbation on the axis of symmetry of the simulation. Any interaction of this axisymmetric perturbation with other perturbations, however, (for example, the interaction of an ablator surface bump with the underlying ice perturbations or other surface bumps) or a non-axisymmetric perturbation is inherently 3-D in character.

Since the low mode perturbations that develop from these surface defects are generally believed to be small enough or sufficiently slowly growing that they remain in the linear regime throughout the

implosion, it is possible to predict and characterize their growth quite universally using growth factors. This technique of predicting implosion perturbations using growth factors has been described at length elsewhere [12]. In short, the growth factors represent the modally decomposed ratio of the amplitudes at some specified surface at a designated time (typically peak velocity or ignition time) to the initial amplitude at some (possibly different) surface. By multiplying an initial surface roughness spectrum by the corresponding growth factor spectrum and then reconstructing the surface from its individual modes, the perturbed surface at the specified time can be projected. Note that the surface at which the perturbation is being projected need not be the surface at which the perturbation is seeded. The growth factor spectrum must simply be defined as corresponding to growth *from* some specified surface *to* another specified surface at the given time. Since the growth is assumed linear, the contributions from initial perturbations on several surfaces, each with its respective growth factor spectrum, may simply be added to obtain the aggregate perturbation at any given surface.

The utility of using growth factors is, of course, that they obviate the need for running a complicated and time-consuming 2-D or 3-D simulation in order to predict the behavior of every implosion. Instead, once the appropriate growth factor spectrum has been obtained (from a single well resolved simulation) and the surface(s) of interest has been characterized, the perturbation amplitudes of the shell at some designated time can be found essentially by merely performing a Fourier transform. On account of this facility, growth factor analysis is being used extensively by the NIC not only to predict implosion performance but also to prioritize which shells are to be used in experiments. On the other hand, the liability of this technique is that it is strictly valid only so long as the perturbation amplitudes remain linear. If, for realistic initial shell surfaces, the perturbations grow to the nonlinear regime, then the development can become fully 3-D and will deviate from the growth

factor prediction. Again, benchmarking against a complete 3-D simulation with realistic initial surfaces is desirable.

To this end, a second 3-D simulation was run using lower resolution but over a larger 45° wedge at the waist. This simulation was run with $1004 \times 512 \times 512$ zones sufficient to resolve Legendre modes $\ell = 4 - 200$ and was initialized with an actual measured shell surface on the outer ablator surface. Power spectral roughness was initialized on all internal surfaces similar to that used in the simulation shown in Fig. 9. A planar projection of the initial outer ablator surface used for this run is shown in Fig. 11 with the color scale giving the surface height in nanometers. A number of bumps, with heights ranging up to 400 nm, as well as a divot surrounded by a trio of bumps can be seen.

The progression of this simulation to peak implosion velocity ($t = 20.98$ ns) is shown by the rendering in Fig. 12 where the color scale now gives the material density. The initial surface perturbations have grown into a number of larger perturbations in the shell several of which, by the criterion of amplitude to wavelength ratio, have reached the weakly nonlinear regime. Despite these large amplitude perturbations, the shell has remained essentially intact without being punctured. The stagnation shock which has begun to arrest the inward motion of the shell is visible as the thin high-density layer in yellow-red rimming the nascent low-density hot spot in blue. Another view of the shell perturbations at peak velocity is given by Fig. 13 which shows the fuel-ablator interface as seen from the ablator side. Comparing to Fig. 11, the initial ablator surface defects are seen to have contributed large spike and bubble perturbations to the fuel-ablator interface. These are superimposed on a lower-level background roughness which results from the broad-spectrum perturbations seeded at the internal interfaces and the ice surface. Again, the large ablator-derived perturbations are at the threshold of nonlinearity when the linear regime growth factor predictions can be expected to break down.

In order to make a quantitative comparison to the growth factor predictions for this implosion, Fig. 14 shows the fuel-ablator interface from Fig. 13 projected flat into the y - z plane (a). The corresponding growth factor prediction is shown in (b). Growth factors similar to those shown in Fig. 4 of Ref. [12] were used to make this prediction. In both, the same color scale is used to give the radial distance of the interface from the center of the implosion. Here, the growth factor prediction includes contributions from the ablator surface defects as well as the initial ice roughness but not the roughness seeded at the internal dopant layers. As such, it is not surprising that the growth factors slightly under predict the total roughness when compared to the 3-D simulation: a 7.8 micron surface RMS as opposed to the 10.1 μm from the simulation. What is surprising, however, is that the overall morphology of the surface is so closely predicted by the growth factors. In both panels, essentially similar constellations of bumps surrounded by troughs appear superimposed on a background of low-amplitude roughness. Again, as can be seen from the color scale, the larger, localized perturbations have grown to amplitudes (several tens of microns) many times their transverse extent (of order ten microns); that is, these perturbations have crossed the threshold of nonlinearity. Evidently, however, growth factors remain an effective predictor for peak velocity perturbations despite the amplitudes of these perturbations having reached what would otherwise be regarded as the nonlinear regime. This conclusion is a reassuring endorsement of the growth factor technique being used by the NIC.

This lower-resolution simulation ran through ignition and burn to give a yield of 17.63 MJ, actually in excess of the 1-D value of 17.27 MJ. Fig. 15 illustrates the state of the hot spot at 21.22 ns, just before the time of 1-D ignition. The left and right boundaries of the rendering in the figure are colored according to the ion temperature and material density, respectively. A central temperature of greater than 7.0 keV has been reached at this point along with a peak density in the compressed shell of more than 900 g/cm^3 . The red surface suspended between the left and right boundaries is the 400

g/cm^3 density isosurface which approximately captures the shape of the igniting hot spot. A number of large, broad bubbles of low-density hot spot can be seen rising into the dense shell with spike sheets of dense material falling between them into the hot spot. The dominant mode number of these hot spot perturbations is in the range of $\ell = 8 - 12$ with a total surface RMS of $4.4 \mu\text{m}$; both of these values are typical of the results from analogous 2-D simulations.

Analogous to Fig. 14, Fig. 16 shows a comparison of the hot spot boundary from the 3-D simulation (a) compared to the result of the hot spot growth factor predictions (b). Again, both are projected into the y - z plane and use the same color scales to give the radial distance of the hot spot boundary from the center of the implosion. In this case, the growth factors are not nearly as effective at predicting the interface shape as they were at peak velocity. While the shapes of the perturbations are generally similar between the 3-D simulation and the growth factor prediction, *i.e.*, the locations of the rising bubbles and falling spikes are generally the same, the growth factor prediction shows much narrower upward going perturbations (bubbles) with higher amplitudes and much more deeply penetrating downward perturbations (spikes) than the simulation. Comparing their respective RMSs, the growth factors over-estimate the hot spot perturbation: $4.4 \mu\text{m}$ versus $5.1 \mu\text{m}$. Apparently, nonlinearity plays a non-negligible role in the exact hot spot shape; nevertheless, in the context of global assessments of capsule performance and ignition probability [12], growth factor prediction can evidently be taken as a conservative upper bounds for the hot spot RMS.

V. High resolution fill tube simulations

A final arena in which the 2-D and 3-D development of hydrodynamic instabilities in ignition capsules can differ is with respect to the jet-type perturbations produced by the fill tube. This glass fill tube is attached to the capsule for the purpose of injecting the DT fuel into the capsule as a liquid

which is then frozen into the cryogenic fuel layer prior to implosion. Previous simulations have demonstrated that in the current Rev. 5 design, the perturbation generated by fill tube can inject approximately 30 ng of doped plastic, as well as fragments of the glass tube itself, through the imploding shell and deep into the central hot spot [11]. This “deep mix” of doped ablator material into the hot spot is an important determinant in the ignition probability of the design; if too much doped material is injected in to the hot spot, from whatever source, the hot spot will radiatively cool and be unable to reach ignition temperatures.

While past simulations have been very highly resolved and included the details of the glue fillet and counter-bore attaching the tube to the capsule, they have all assumed 2-D rotational symmetry. On the other hand, radiographs of prototype capsules have shown, not unsurprisingly, that drilled fill holes are neither perfectly straight (*i.e.*, aligned with the axis of rotation of the capsule) nor perfectly smooth. The drilled holes can in fact be tilted $\sim 1^\circ$ from the axis and have variations in diameter of the order of a few percent down the length of the tube (*i.e.*, bumps) as well as taper from the outer end of the fill hole to the inner end. The tilt of the tube is, of course, an exclusively 3-D characteristic and the bumps can also be 3-D. What is more, the high-aspect ratio jets which the fill tube and fill hole have been shown to produce in 2-D could be unstable to kinking in 3-D or the development of 3-D shock-induced turbulence, *e.g.* [21]. Any deviations from axisymmetry can, of course, seed these instabilities, and these in turn might be expected to reduce the penetrability of the jet. So as accurately to understand the susceptibility of capsule designs to deep mix from the fill tube, a 3-D benchmarking of 2-D axisymmetric fill tube simulations is needed.

For these fill tube simulations, the 3-D code used for benchmarking 2-D HYDRA simulations was chosen to be the high-order Eulerian code Miranda [22]. Miranda solves the multi-material hydrodynamics equations on a 3-D Cartesian mesh including heat conduction and grey radiation

diffusion. Given the different capabilities of HYDRA and Miranda, in order to make a useful comparison, the following simplified test problem was then constructed: The spherical capsule was approximated as a 75 μm thick slab of DT ice backed by a 153 μm slab of beryllium to which a 100 μm long, 10 μm diameter glass fill tube is attached. (These “shell” dimensions correspond to an earlier beryllium ablator version of the ignition capsule design.) The inner fill tube diameter is 5 μm and matches to the 5 μm diameter hole perforating the beryllium ablator. A 20 μm deep counter bore seats the fill tube into the beryllium slab. The fill hole and tube are filled with DT ice, and the latter is capped with a 20 μm glass slug to prevent unphysical radiation leakage through the fill tube and hole into the fuel layer. Finally, the single-temperature radiation drive is sourced into an annulus 100 μm from the ablator surface. As a function of time, the radiation pulse rises steeply to a plateau of 68 eV and maintains this value for 15 ns; this profile roughly approximates the “foot” of the detailed radiation drive for the original capsule design.

When HYDRA was run with the same physics settings as Miranda (material opacities and equations-of-state, grey radiation diffusion, flux-limited conduction, etc.) a good match of the 1-D density, pressure, and temperature profiles was achieved between Miranda and HYDRA. This match then served as the basis for comparing a 2-D HYDRA simulation of the axisymmetric fill tube and hole to a 3-D Miranda simulation. For the latter, the 3-D effect of a 1.72° tilt was added to the fill hole as well as a taper from an 8 μm hole diameter at the outside of the ablator to a 5.2 μm diameter at the inside and a random set of bumps representative of those seen in prototype radiographs.

Fig. 17 shows a comparison of the 3-D Miranda results against the 2-D HYDRA results. In (a), three snapshots in time are shown where the 3-D Miranda results are “sliced” in the plane of the tilted fill hole. The color scale gives the density with blue characterizing unperturbed DT ice, green the unperturbed beryllium shell, and orange-yellow the shocked beryllium. (b) is an equivalent

comparison but slicing the Miranda results out of the plane of the tilt. As an indication of the matching achieved between the 1-D hydrodynamics, the location of the shock traversing the beryllium into the DT tracks closely between the Miranda and HYDRA results. What is noticeably different in 1-D between Miranda and HYDRA is the thickness of the ablation front at the top of each panel with the HYDRA ablation front much thicker than Miranda. This is due to the need to relax the mesh in the ablating zones in the HYDRA simulation, in order to avoid mesh tangling from the fill tube perturbation, but does not appear to impact the shock strength or speed in the slab.

In (a), the initial tilt of the fill tube is apparent in the unshocked beryllium (at $t = 5.0$ ns), and this tilt appears to imprint on the subsequent jet evolution into the DT fuel. In the 2-D axisymmetric HYDRA simulation, the jet, of course, travels directly down the tube. Despite this slight directional difference, the 3-D and 2-D jets appear to propagate at nearly the same rate and both reach the edge of the DT ice (the bottom of each panel in the figure) at 10.0 ns. Limited computation resources prevented continuing the comparison past $t = 10.0$ ns. In addition to the tilt, the fine scale structure within the jet due to the roughness applied to the 3-D fill hole is evident in both (a) and (b). Again, while this 3-D perturbation adds structure to the interior of the jet, the jet propagation distance and lateral expansion are essentially equivalent between 2-D and 3-D.

As a more quantitative comparison of the jet evolution, Fig. 18 compares the cumulative injected mass (integrated transversely and as a running integral in the longitudinal direction) as a function of longitudinal distance from the Miranda and HYDRA simulations. The solid curves give the result from the Miranda simulation and the dash-dot curves give the result from HYDRA. The cluster of lines to the left give the injected beryllium mass, and the curves in the lower right show the injected glass from the fill tube, both shown at 8.0 and 10.0 ns. The leading plateaus in the beryllium curves give the total integrated mass in the fill hole jet with the subsequent steep rise corresponding to the

location of the beryllium-DT interface. While the agreement is not perfect, 2-D HYDRA and 3-D Miranda both predict approximately 20 ng of beryllium injected by 10.0 ns and to approximately the same depth in the DT. The mass of glass injected from the fill tube differs by a factor of a few between 2-D and 3-D, but given that neither simulation predicts more than a fraction of a nanogram is injected, this discrepancy should have no consequence for ignition. As regards the mass of beryllium injected by the fill tube perturbation, these results can be taken as a validation that 2-D simulations are adequate to capture the fill hole jet dynamics.

VI. Conclusions

This paper has summarized a number of recent high-resolution, 2-D and 3-D simulations run to quantify the performance of the current NIF ignition capsule design and some of the design modifications motivated by these simulations. With regard to the high-mode mixing at the fuel-ablator interface, a series of 2-D high-resolution simulations was used to re-optimize the dopant concentration and distribution leading to the current Rev. 5 capsule design. Following the re-optimization, the fraction of the fuel mass uncontaminated by ablator, the figure of merit for this high-mode mix of ablator material into the DT fuel, increased substantially from the previous 0.21 clean fraction to 0.77. This re-design was spurred by the first series of experimental results from NIF indicating higher hohlraum hard x-ray fractions than had been anticipated and used in previous capsule optimizations.

The re-optimization based on 2-D high-resolution simulations was then benchmarked against an analogous high-resolution 3-D simulation. Slightly more nonlinear development of the mix layer was found in the 3-D simulation when compared to 2-D, but the interface perturbations remained coherent (*i.e.*, not turbulent) and the fuel clean fraction was not substantially different in 3-D than in 2-D.

Likewise, a lower-resolution 3-D simulation run over a larger sector of the capsule was used as a benchmark for the linear growth factor analysis being used to predict the performance of fabricated ablator shells to be used for NIF experiments. The growth factor predictions were found to compare very well with the full 3-D simulation at peak velocity though were less successful in predicting the hot spot shape at ignition time. These results validate the use of growth factors in predicting peak velocity growth for realistic implosion targets and show that they provide an upper bound for hot spot growth. Finally, a comparison was made between a 3-D simulation of the fill tube-induced jet developing in a simplified test problem with an analogous 2-D axisymmetric simulation. While the 3-D simulation showed more internal structure to the jet, the overall propagation rate of the jet, the lateral extent of the jet, and the total mass of ablator material injected by the jet were well matched by the 2-D axisymmetric simulation. Again, these results serve to benchmark the 2-D simulations used on a production basis to design and evaluate capsule performance.

ACKNOWLEDGEMENT. This work was performed under the auspices of the U.S. Department of Energy by Lawrence Livermore National Laboratory under Contract DE-AC52-07NA27344.

References

- [1] G. H. Miller, E. I. Moses, and C. R. Wuest, *Nuc. Fusion* **44**, S228 (2004).
- [2] J. D. Lindl, P. A. Amendt, R. L. Berger, *et al.*, *Phys. Plasmas* **11**, 339 (2004).
- [3] E. I. Moses, R. N. Boyd, B. A. Remington, C. J. Keane, and R. Al-Ayat, *Phys. Plasmas* **16**, 041006 (2009).
- [4] S. H. Glenzer, B. J. MacGowan, P. Michel, *et al.*, *Science* **327**, 1228 (2010).
- [5] O. Landen, J. Edwards, S. W. Haan, *et al.*, *Phys. Plasmas*, *submitted*.
- [6] D. H. Munro, P. M. Celliers, G. W. Collins, *et al.*, *Phys. Plasmas* **8**, 2245 (2001).
- [7] B. A. Hammel, H. A. Scott, C. Cerjan, *et al.*, *Phys. Plasmas*, *submitted*.
- [8] F. Hattori, H. Takabe, and K. Mima, *Phys. Fluids* **29**, 1719 (1986).
- [9] D. Layzer, *Astrophys.* **44**, 1 (1955).
- [10] J. Edwards, M. Marinak, T. Dittrich *et al.*, *Phys. Plasmas* **12**, 056318 (2005).
- [11] B. A. Hammel, S. W. Haan, D. S. Clark *et al.*, *High Energy Density Physics* **6**, 171 (2010).
- [12] S. W. Haan, J. D. Lindl, D. A. Callahan, *et al.*, *Phys. Plasmas*, *submitted*.
- [13] D. S. Clark, S. W. Haan, B. A. Hammel, J. D. Salmonson, D. A. Callahan, and R. P.J. Town, *Phys. Plasmas* **17**, 052703 (2010).
- [14] R. P. J. Town, M. D. Rosen, P. A. Michel, *et al.*, *Phys. Plasmas*, *submitted*.
- [15] M. M. Marinak, G. D. Kerbel, N. A. Gentile, *et al.*, *Phys. Plasmas* **8**, 2275 (2001).
- [16] G. B. Zimmerman and W. L. Kruer, *Comments Plasma Phys. Controlled Fusion* **2**, 51 (1975).
- [17] G. B. Zimmerman and R. M. More, *J. Quant. Spectrosc. Radiat. Transfer* **23**, 517 (1980).
- [18] R. M. More, *J. Quant. Spectrosc. Radiat. Transfer* **27**, 345 (1982).
- [19] H. A. Scott and S. B. Hansen, *High Energy Density Physics* **6**, 39 (2010).
- [20] J. D. Salmonson, private communication (2007).

- [21] O. A. Hurricane, J. F. Hansen, and H. F. Robey, Phys. Plasmas **16**, 056305 (2009).
- [22] A. W. Cook, Phys. Fluids **19**, 055103 (2007); Phys. Fluids **21**, 055109 (2009).

Figure captions

Fig. 1. “Pie diagram” of the current Rev. 5 ignition capsule design. The dopant concentrations and layer thicknesses shown in the figure result from the re-optimization described in Sec. 2.

Fig. 2. Hohlraum hard x-ray fraction (fraction of x-ray radiation at an energy greater than 1.8 keV) versus radiation temperature. The diamonds correspond to NIF measurements, the squares to integrated hohlraum simulations of those experiments run with HYDRA, and the circles to integrated simulations run with Lasnex. The solid curve plots the hard x-ray fraction from an x-ray source spectrum used to drive high-resolution capsule simulations extracted from a Lasnex hohlraum simulation. The dashed curve is the analogous hard x-ray fraction from a HYDRA-derived x-ray source, and the dash-dot curve shows the result of multiplying the hard x-ray fraction of that source by a factor of 1.2. The latter curve reasonably reproduces the hard x-ray fractions from the experimental data base and was used for the high-resolution capsule simulations used in re-optimizing the capsule design.

Fig. 3. Comparison of density profiles during the acceleration phase for the current Rev. 5 design (solid) and the previous Rev. 4 design (dashed) driven by the updated x-ray source. The notch in each profile corresponds to the interface between the dense DT fuel to the left and the lower density plastic ablator to the right. With the updated x-ray source, the previous Rev. 4 design has an unacceptably large Atwood number at this interface leading to substantial mixing of ablator material into the fuel.

Fig. 4. Roughness power spectra versus Legendre mode number as used in high-resolution capsule simulations. The spectra represent fits to measured shell roughnesses as well as constraints found necessary on the roughness based on simulations.

Fig. 5. (Color online) High-resolution 2-D simulation of the current Rev. 5 capsule design shown at peak implosion velocity. The material region is shown on the left half of the panel and the density on the right half. This simulation was run on a 15° wedge at the capsule waist with 1217×1024 zones in the radial and angular directions, respectively. The resolution is sufficient to capture Legendre mode numbers of $\ell = 12 - 1,200$. The fuel-ablator interface separates the dark blue from the light blue regions. Mixing at this interface results in a fuel clean mass fraction of 0.77 at peak velocity.

Fig. 6. (Color online) High-resolution 2-D simulation of the previous Rev. 4 capsule design using an updated x-ray source. The simulation parameters and resolution are similar to those of Fig. 5. The higher fuel-ablator Atwood number for this implosion as compared to Rev. 5 (see Fig. 3) results in the unacceptable degree of mix between the fuel and ablator. As a result of this mixing, the fuel clean fraction has been reduced to 0.21 at peak velocity.

Fig. 7. Summary of high-resolution capsule simulations plotted in the plane of fuel clean fraction at peak velocity versus peak ablator dopant concentration. The open circles correspond to capsule designs at the 1.55 MJ scale (Rev. 4) and the filled symbols to designs at the 1.3 MJ scale (Rev. 5). By successively increasing the ablator dopant concentration and increasing the fuel and ablator thicknesses, the fuel clean fraction can be raised from 0.21 (Rev. 4) to the 0.77 of the current Rev. 5 design. The effects of the uncertainties in the measured hard x-ray fraction and in the ablator dopant concentration as

fabricated are represented by the error bars. Note that the clean fraction reaches a local maximum at 1.0 at. % Ge and decreases when the concentration is increased further to 1.2 at. %.

Fig. 8. (Color online) Results at peak velocity of seeding roughness on selected interfaces only in the current Rev. 5 design: (a) seeding roughness at the inner ice surface only, (b) seeding the fuel-ablator interface only, (c) seeding the internal dopant layers only, and (d) seeding the outer ablator surface only. Seeding at the outer ablator surface results in instability growth predominantly in the relatively long wavelength range of $\ell \cong 30$, but is the largest contributor to the mix fraction of ablator material into the fuel.

Fig. 9. (Color online) 3-D high-resolution simulation of Rev. 5 shown at peak velocity. This simulation was run on a $2.5^\circ \times 2.5^\circ$ patch at the capsule waist with $1006 \times 256 \times 256$ zones in the radial and angular directions, respectively, and resolves modes $\ell = 72 - 1,200$. The resulting peak velocity fuel clean fraction is 0.76, very close to the analogous 2-D result of 0.77. Note, however, that due to the limited angular extent that can be simulated in 3-D (2.5° versus 15°), this simulation cannot resolve the $\ell \cong 30$ growth which is a substantial contributor to the mix fraction. Nevertheless, that the mix layer remains coherent and does not develop turbulence in 3-D suggest that the 2-D simulations should be approximately correct in optimizing the mix.

Fig. 10. (Color online) Fuel-ablator interface from the 3-D high-resolution simulation of Fig. 9: (a) seen from the ablator side, and (b) seen from the fuel side. From the fuel side, mushroom-like structures can be seen around the tips of the bubbles of low density ablator material rising into the higher density

fuel. This is uncharacteristic of coupled Rayleigh-Taylor-Kelvin-Helmholtz instabilities where the mushroom-like structures typically appear around the spike tips and not the bubble heads.

Fig. 11. (Color online) Initial outer ablator surface used in a 3-D lower resolution simulation of Rev. 5 (see Fig. 12). The surface is taken from a measurement of a fabricated prototype shell and includes a number of bumps and divots ranging up to 400 nm in height.

Fig. 12. (Color online) 3-D lower resolution simulation of Rev. 5 at peak implosion velocity. The color scale gives the density. This simulation includes $1004 \times 512 \times 512$ zones and resolves modes $\ell = 4 - 200$. In addition to the outer ablator roughness (Fig. 11), power spectrum roughness was initialized on the inner ice surface, the inner ablator surface, and all internal interfaces. Nonlinearly large perturbations have grown up, visible in the dense red-colored region, though they have not broken through the shell.

Fig. 13. (Color online) The fuel-ablator interface at peak velocity from the simulation of Fig. 12 as viewed from the ablator side. The initial ablator defects (Fig. 11) have produced a number of pronounced features at the fuel ablator interface of nonlinear amplitudes.

Fig. 14. (Color online) Comparison of height maps of the fuel ablator interface at peak velocity from (a) the 3-D simulation (cf. Fig. 13) and (b) the prediction of linear growth factors. The color scale gives the radial location of the interface from the implosion center and is the same in both (a) and (b). The agreement is remarkably close between the growth factor prediction and the simulation result, despite the perturbation amplitudes having reached weakly nonlinear amplitudes.

Fig. 15. (Color online) Hot spot shape close to ignition time from the simulation of Fig. 12. The left and right boundaries of the simulation domain show the ion temperature and material density, respectively. The red surface traces the 400 g/cm^3 density isosurface which approximately captures the shape of the igniting hot spot. Large upward going bubbles and downward falling spike sheets are evident at the hot spot boundary. Despite these perturbations, the simulation ignited to give a yield of 17.63 MJ.

Fig. 16. (Color online) Comparison of height maps of the hot spot shape from the 3-D simulation (cf. Fig. 15) and hot spot growth factor predictions. The hot spot growth factors can be used as an upper bound on the hot spot surface RMS but do not capture the detailed hot spot shape as well as they do the peak velocity fuel-ablator interface shape. The effect of nonlinearities are apparently non-negligible for the hot spot.

Fig. 17. (Color online) Comparison of 3-D Miranda and 2-D HYDRA simulations of a fill tube test problem at selected times: (a) in the plane of the 3-D fill hole tilt and (b) out of the plane of tilt. The 3-D Miranda simulation includes a tilt to the fill hole of 1.72° , a taper to the fill hole from $8 \text{ }\mu\text{m}$ to $5.2 \text{ }\mu\text{m}$, and fill hole roughness. Despite these perturbations, the 2-D HYDRA simulation quite closely captures the propagation rate and lateral expansion of the jet generated by the fill tube perturbation.

Fig. 18. Comparison of injected ablator and glass fill tube mass from the Miranda (solid) and HYDRA (dash-dot) simulations shown in Fig. 17. The cluster of lines to the left give the integrated mass of ablator material in the simulation domains (integrated transversely and as a running integral in the axial

direction) as a function of axial distance, and the cluster of lines in the lower right give the integrated mass of glass. Both simulations are in reasonable agreement on the mass included in the fill tube jet (~20 ng at 10.0 ns) but show a factor of a few discrepancy in the mass of glass injected.

Fig. 1

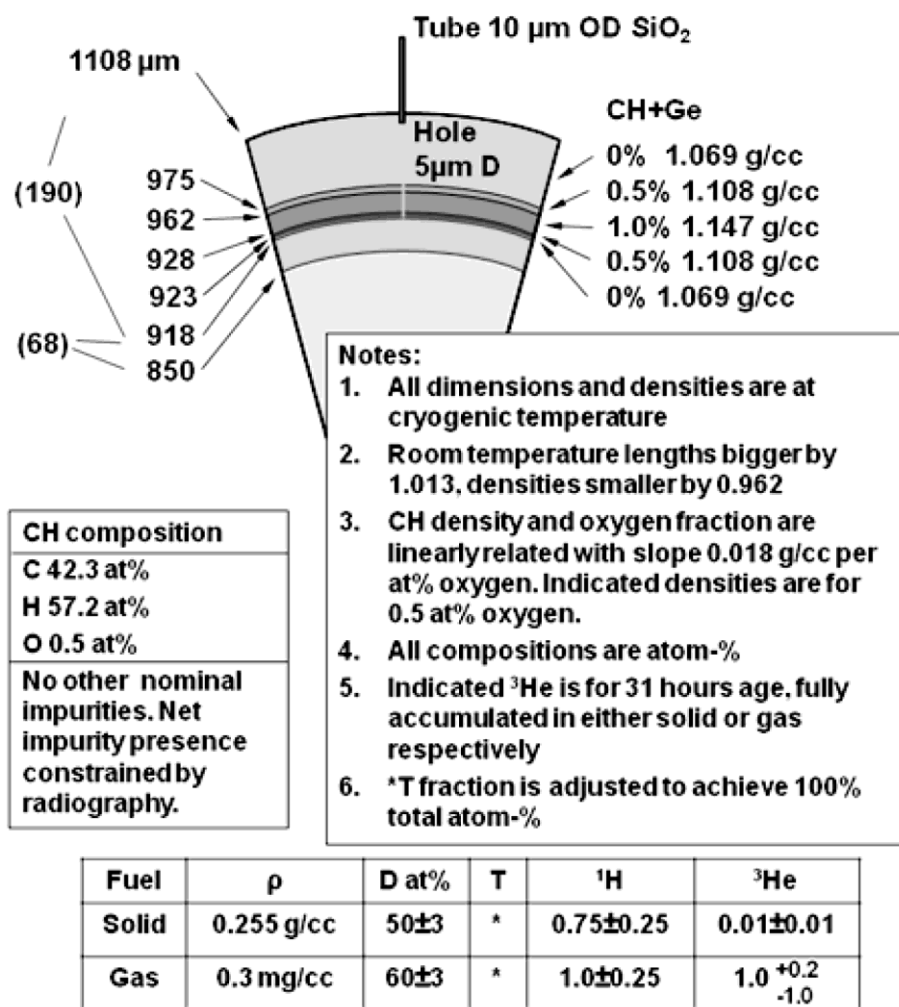


Fig. 2

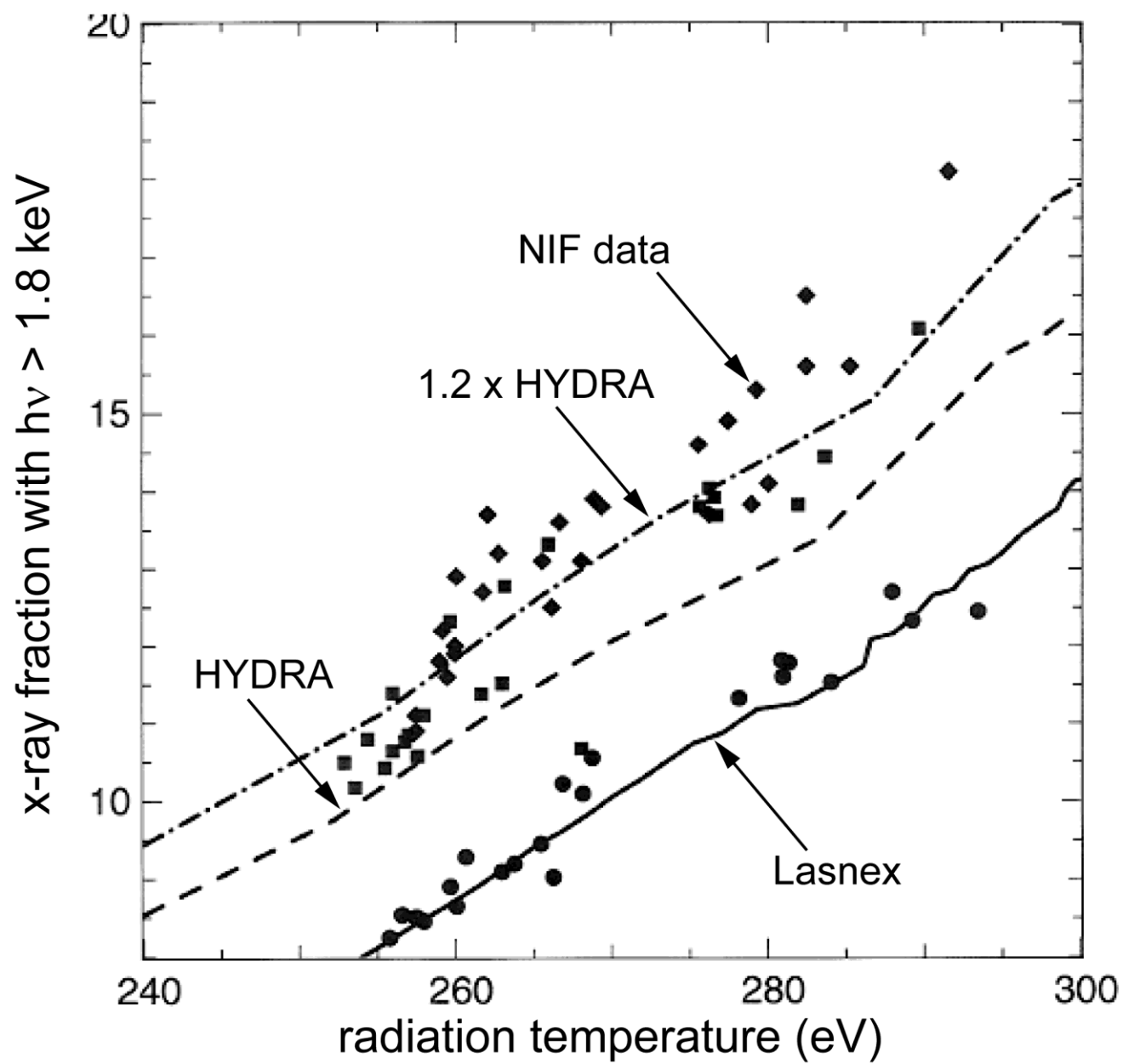


Fig. 3

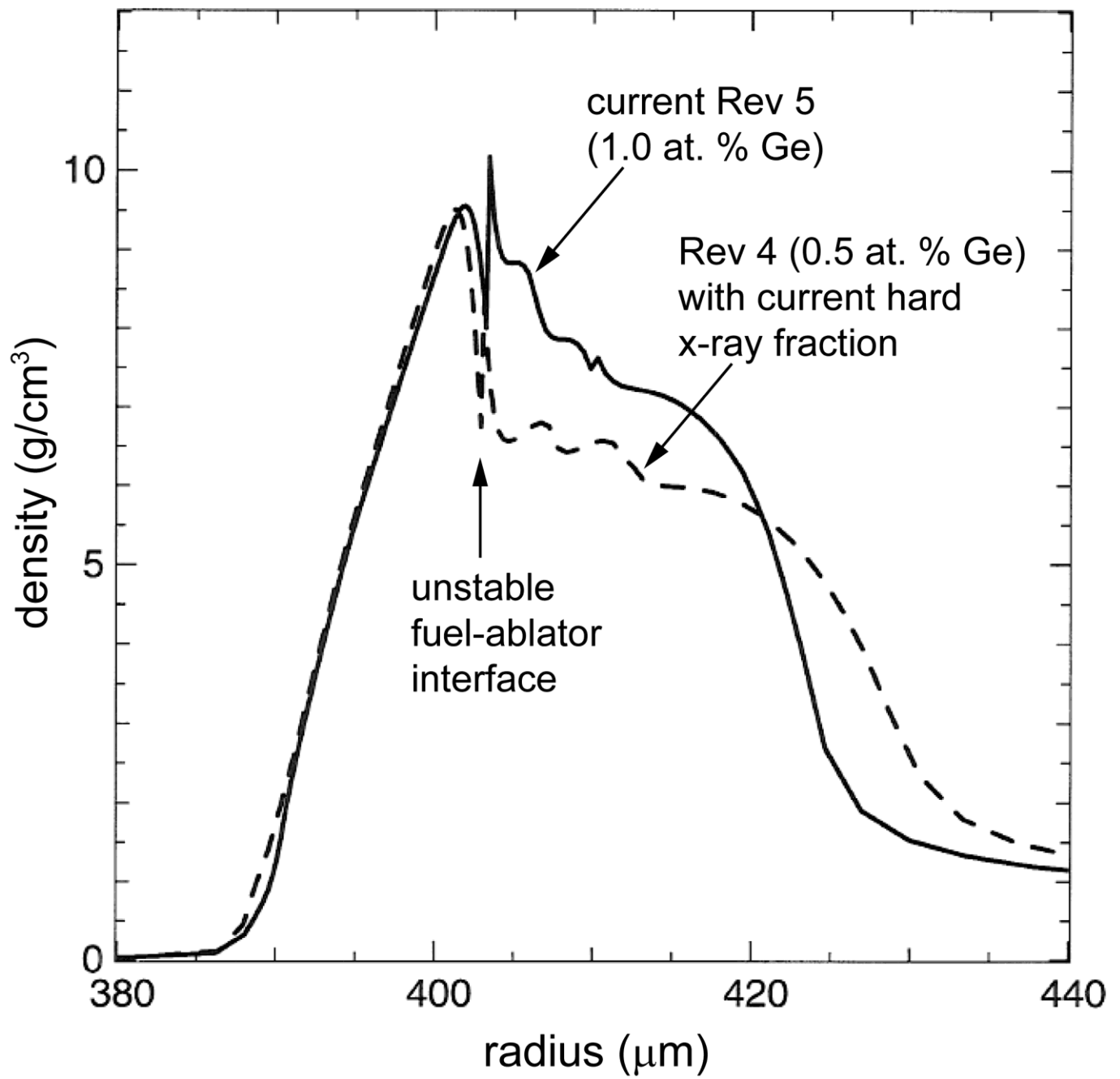


Fig. 4

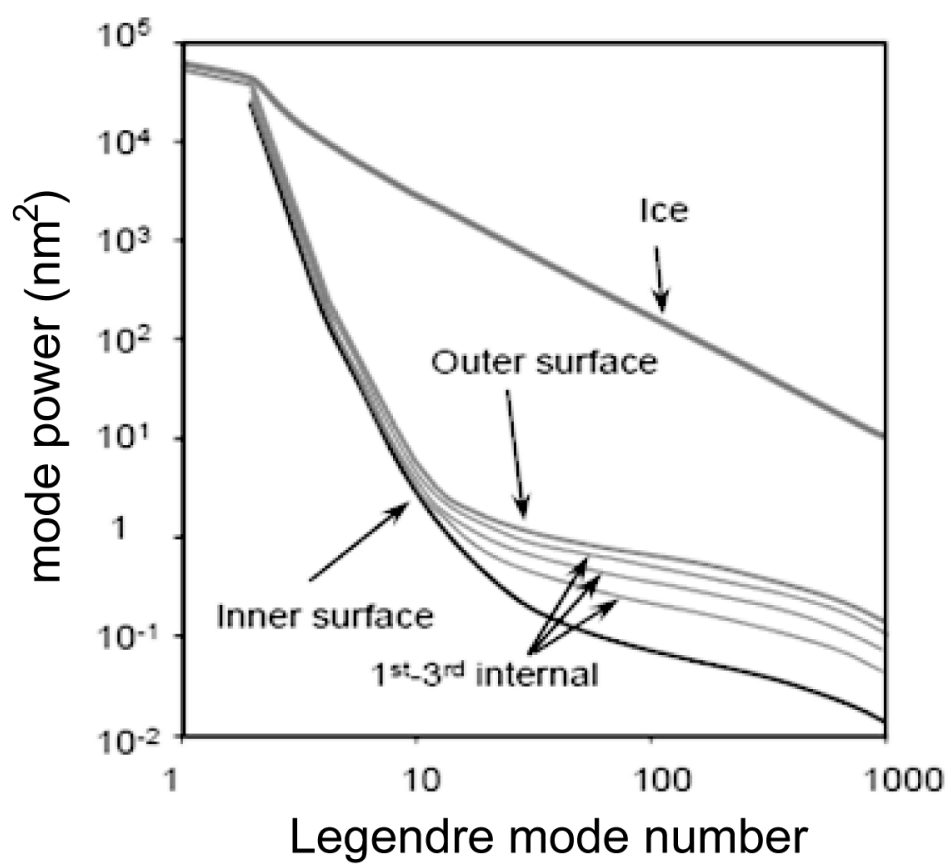


Fig. 5

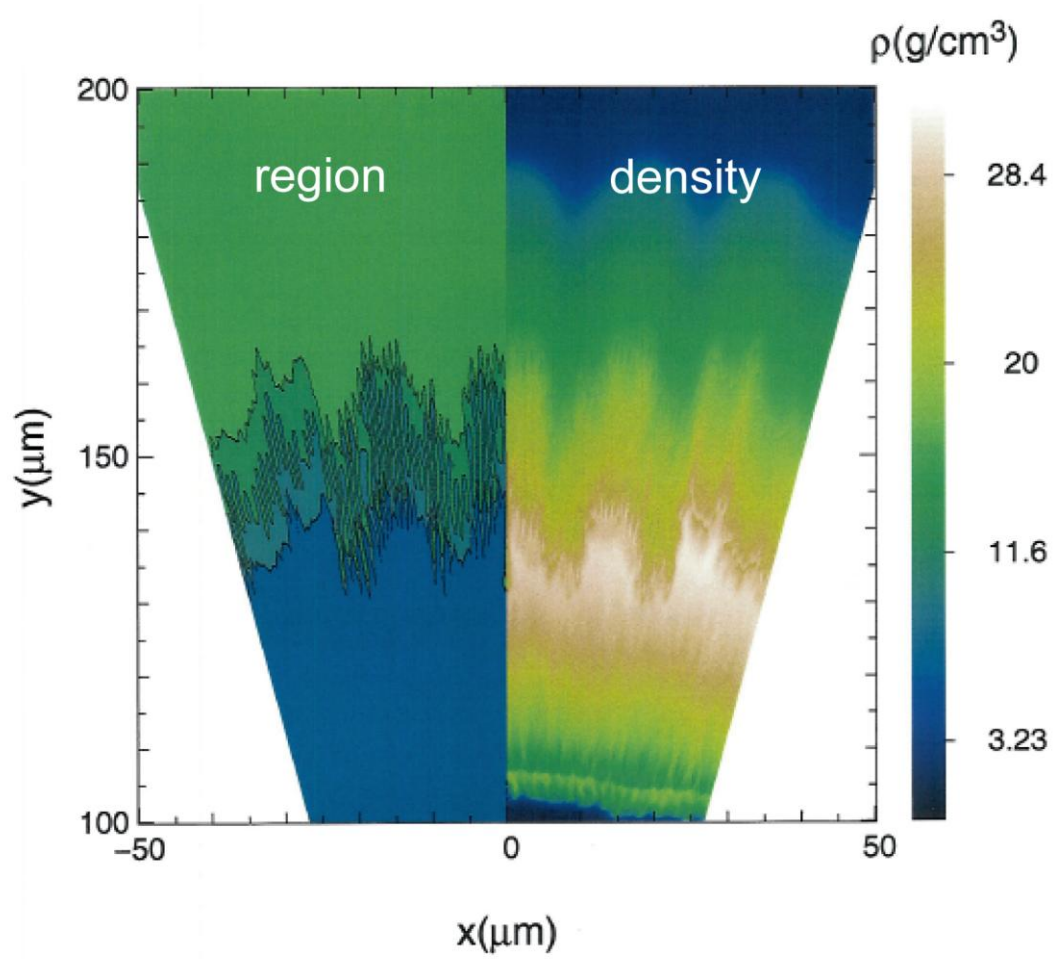


Fig. 6

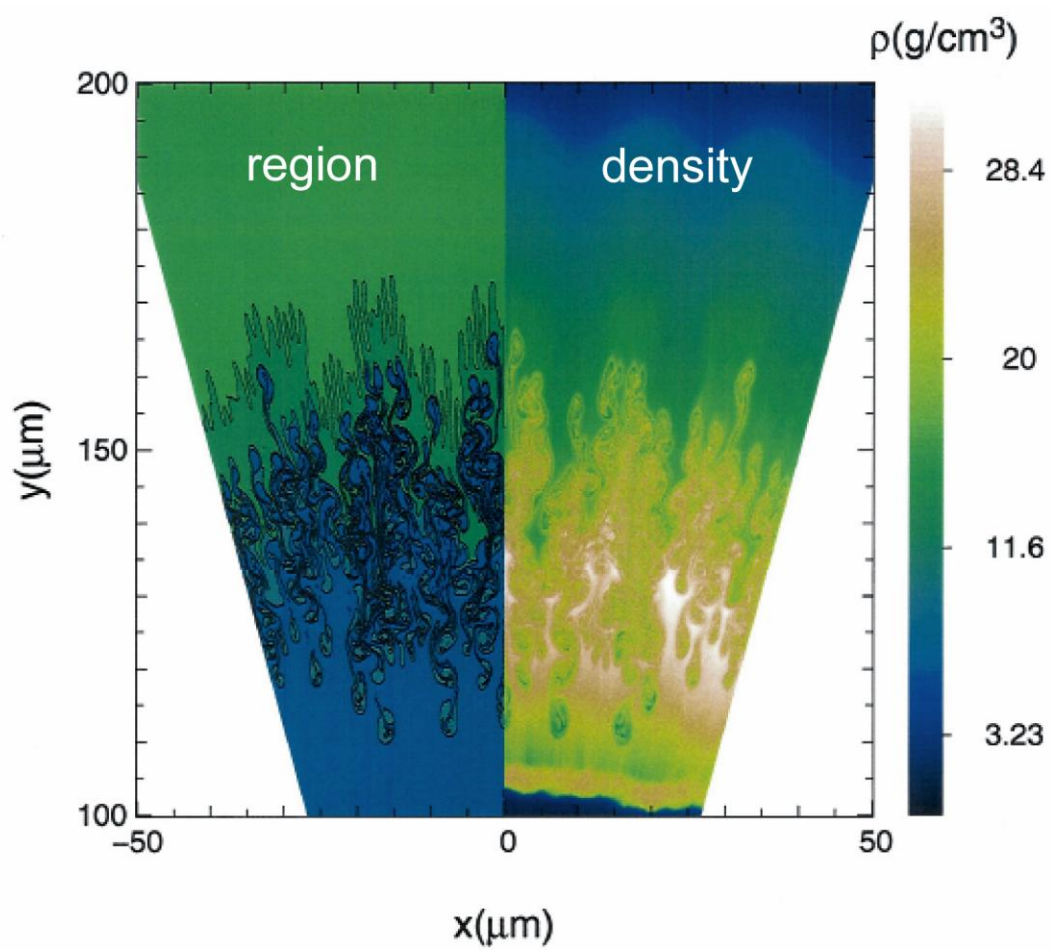


Fig. 7

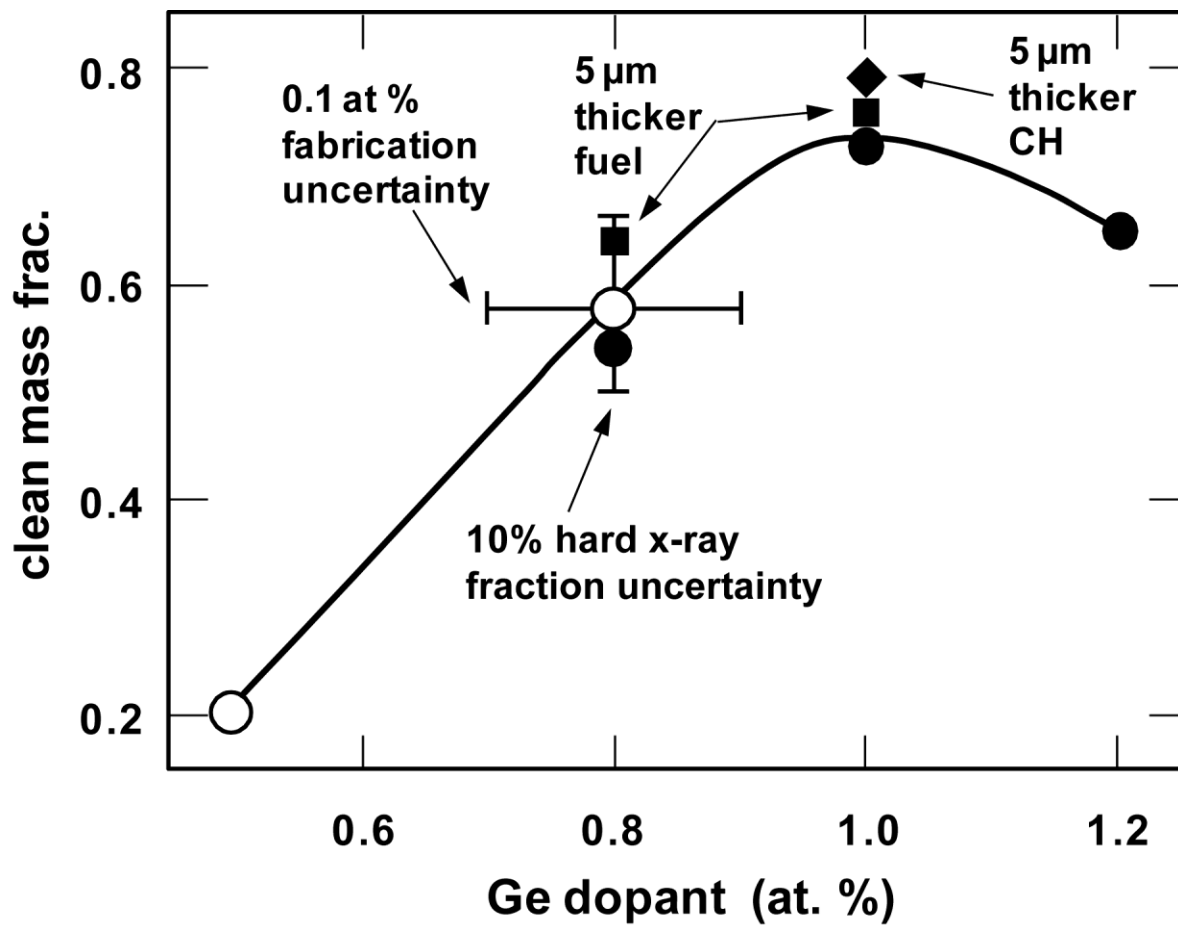


Fig. 8

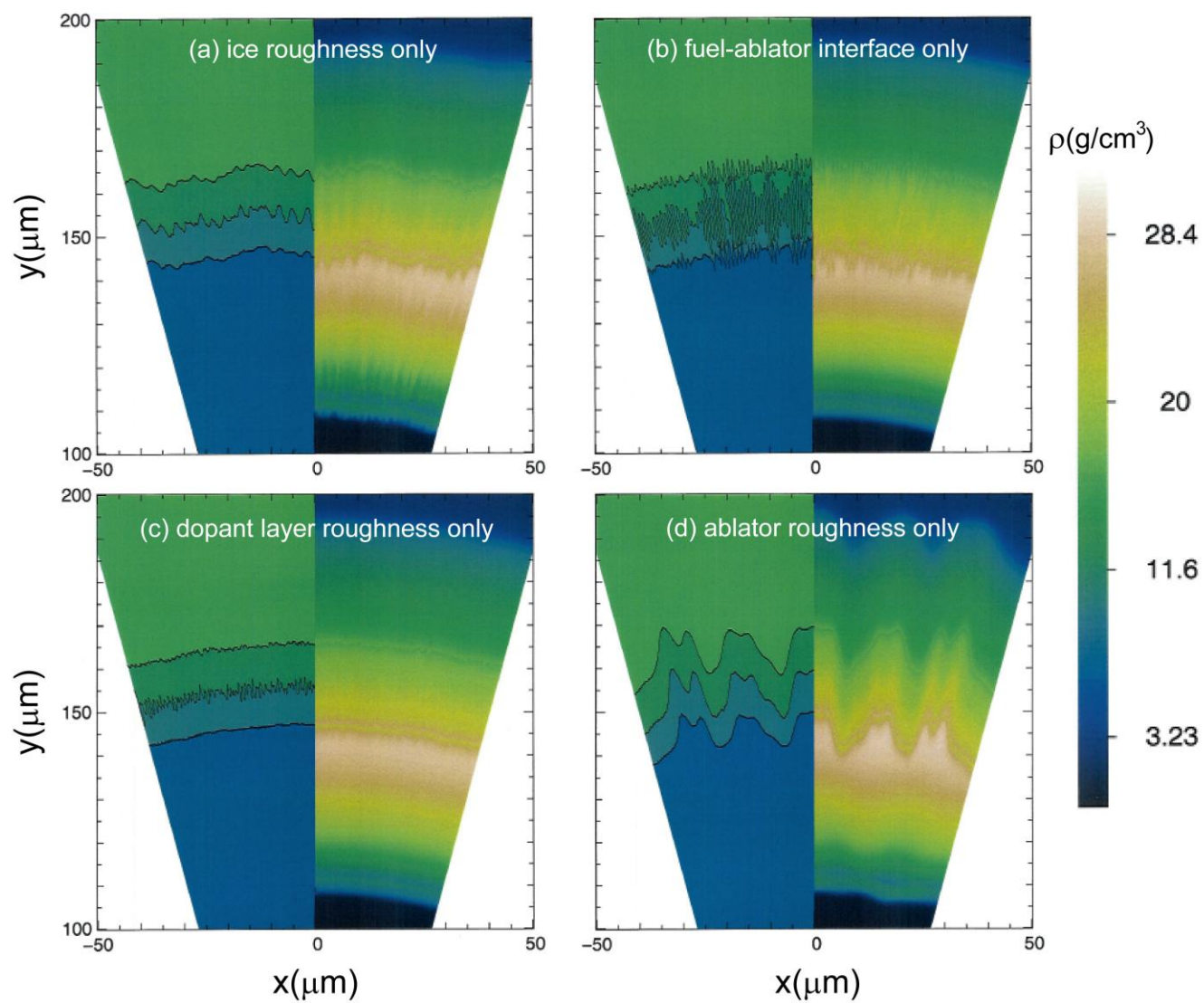


Fig. 9

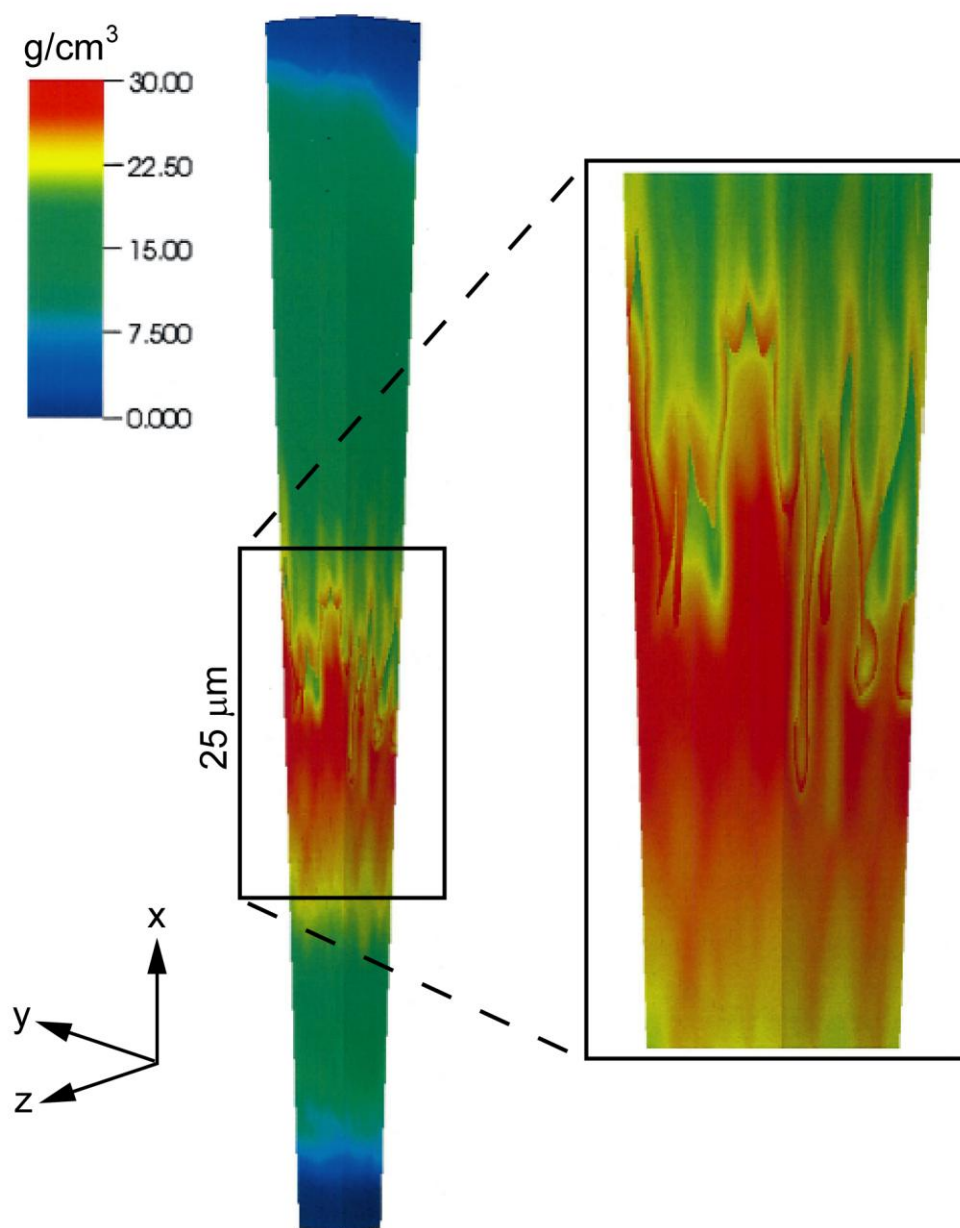


Fig. 10

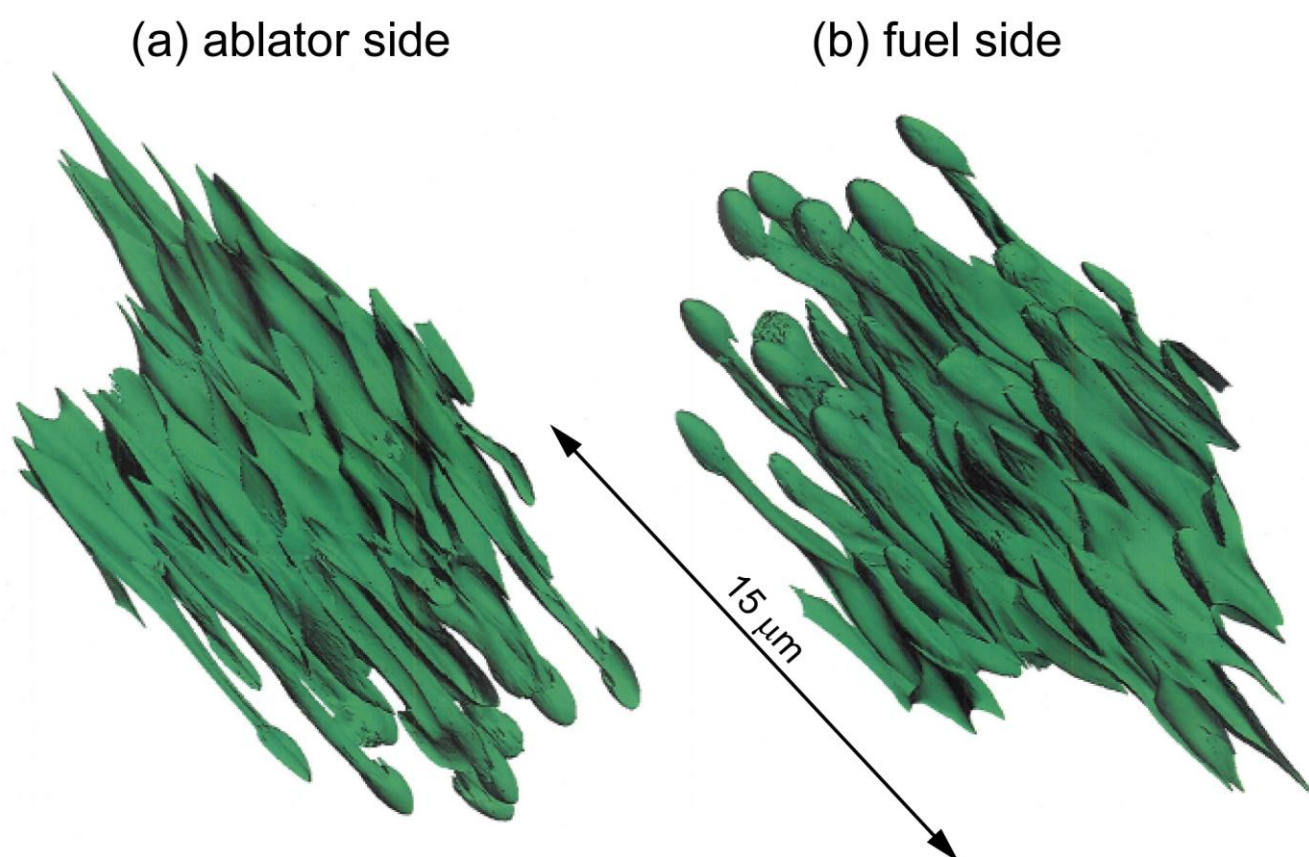


Fig. 11

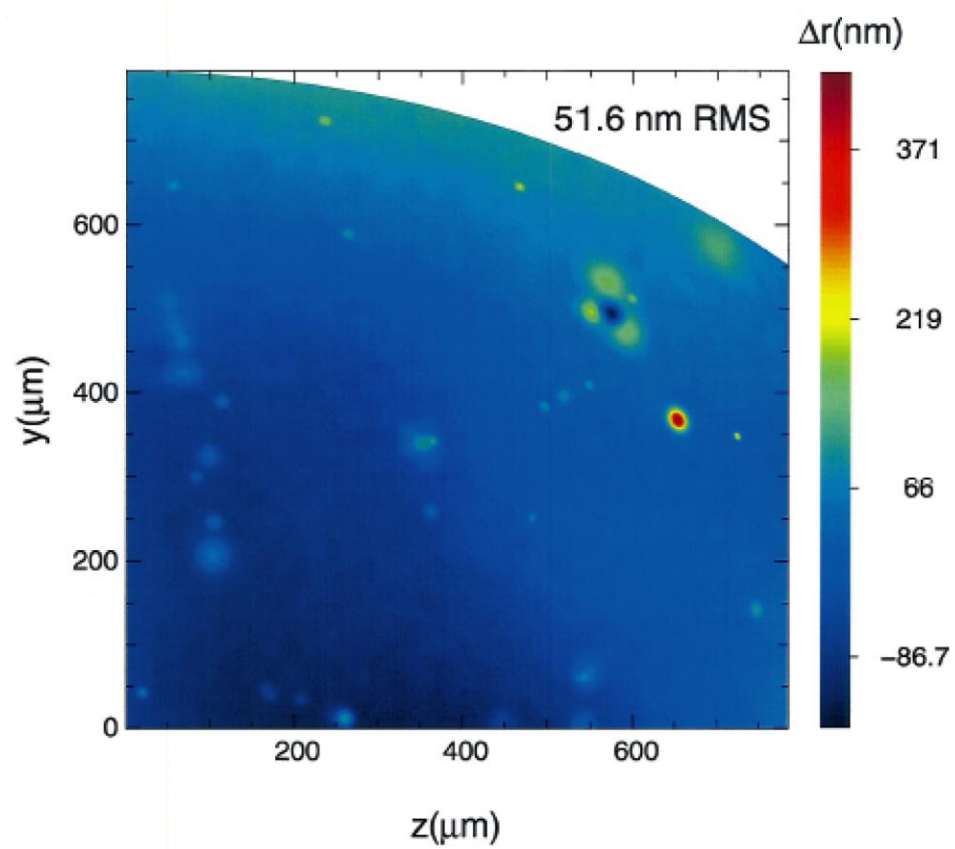


Fig. 12

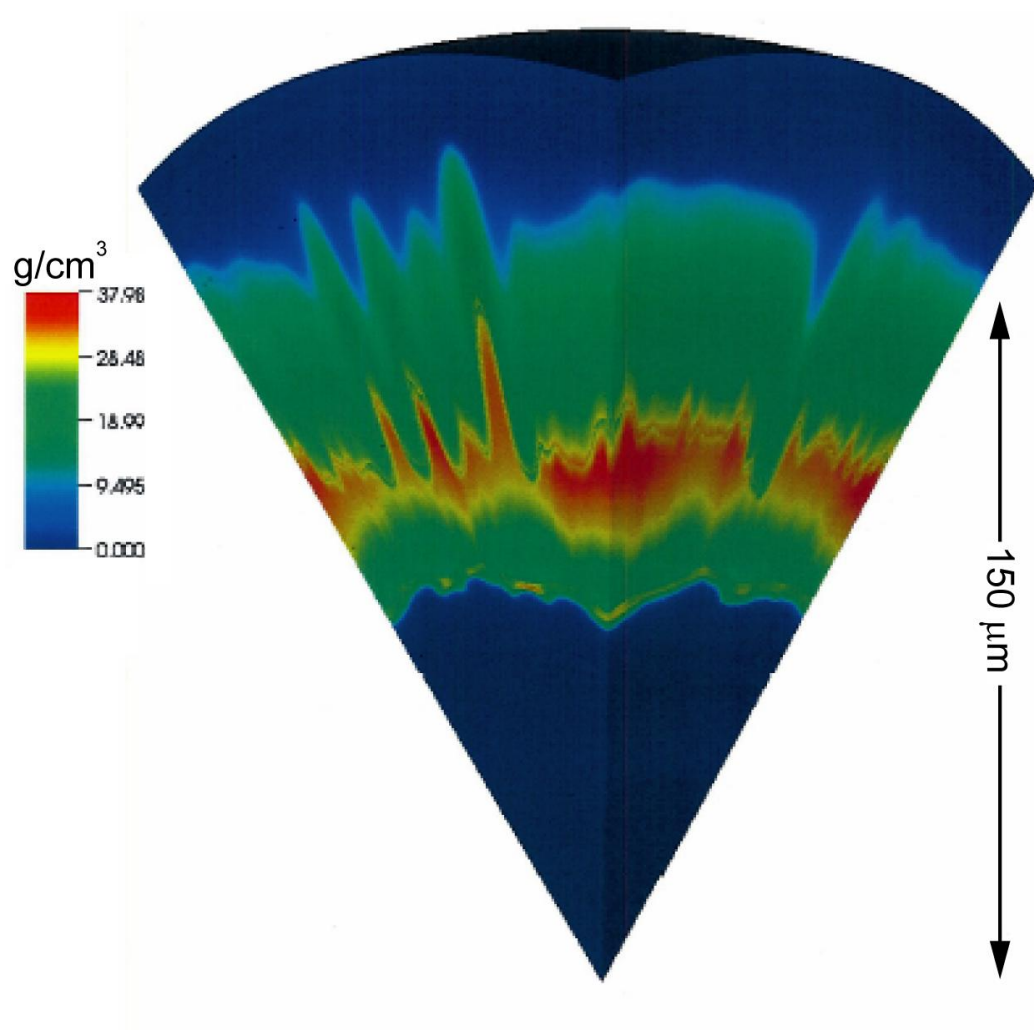


Fig. 13

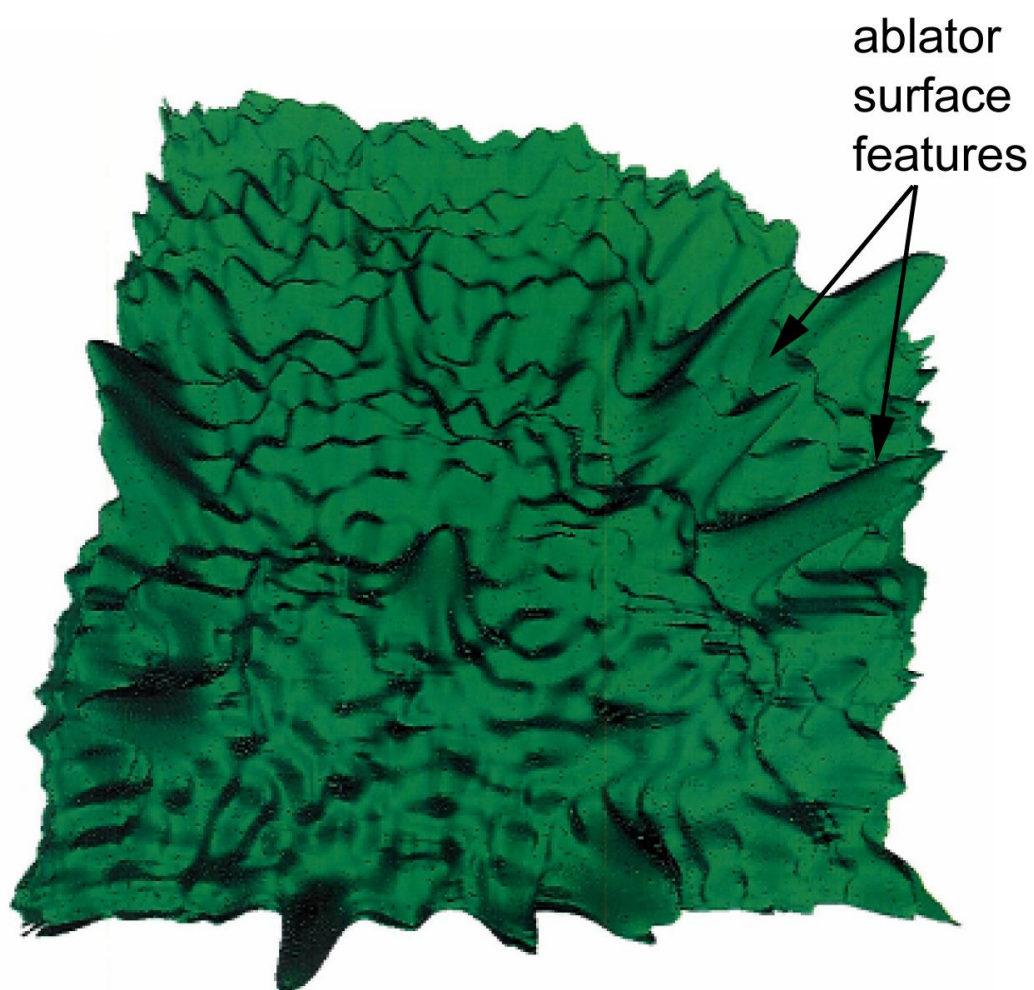


Fig. 14

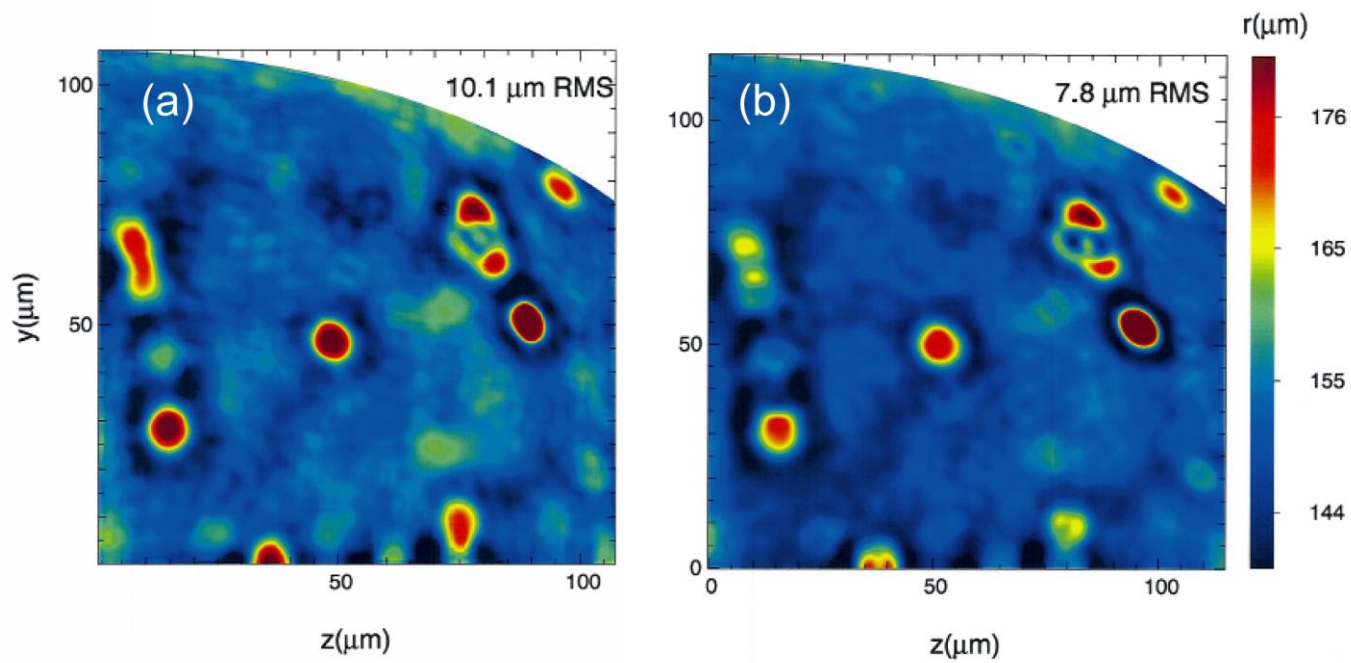


Fig. 15

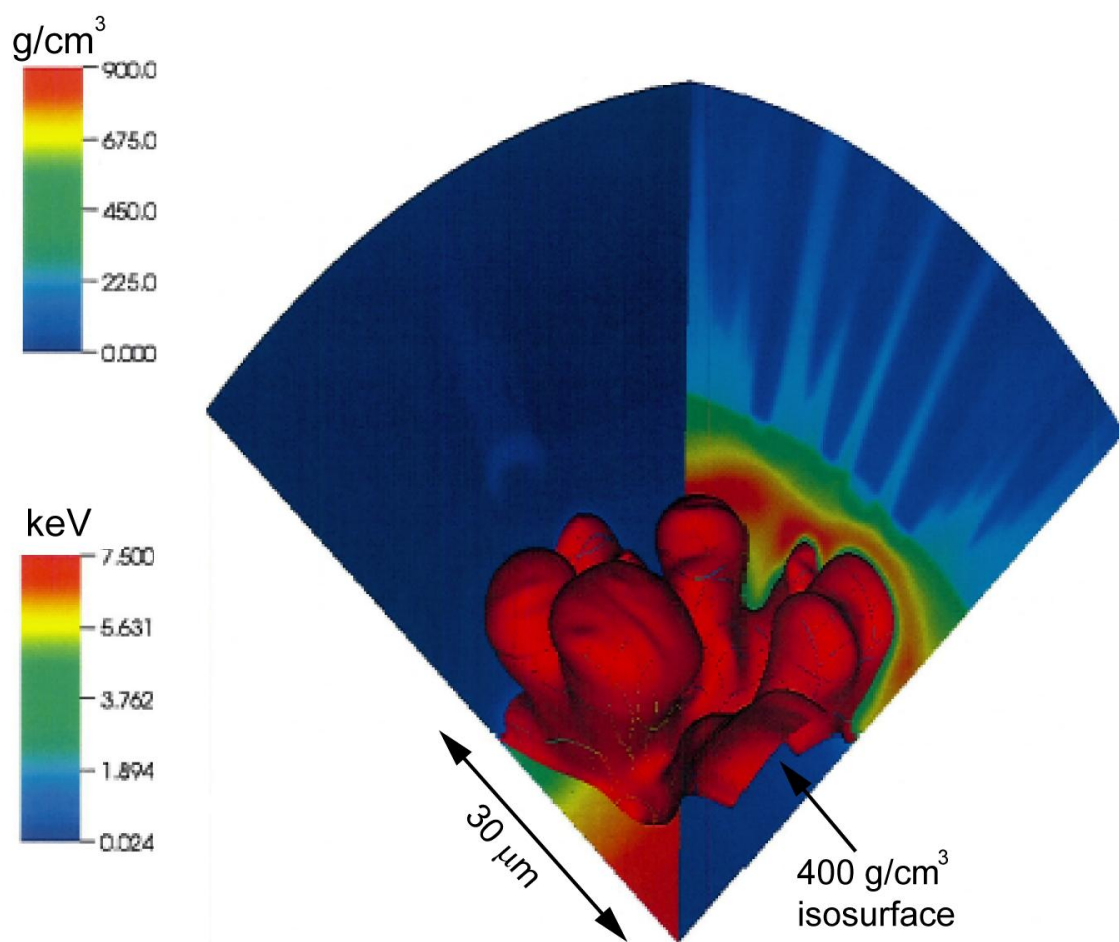


Fig. 16

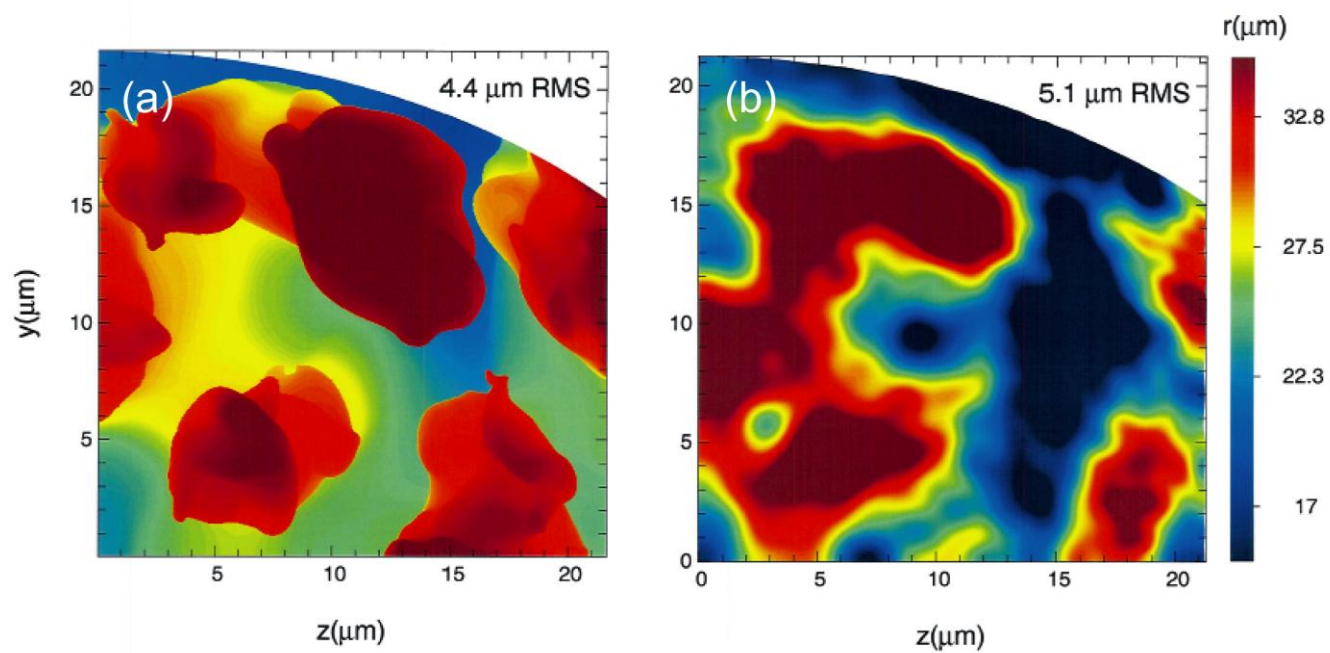


Fig. 17

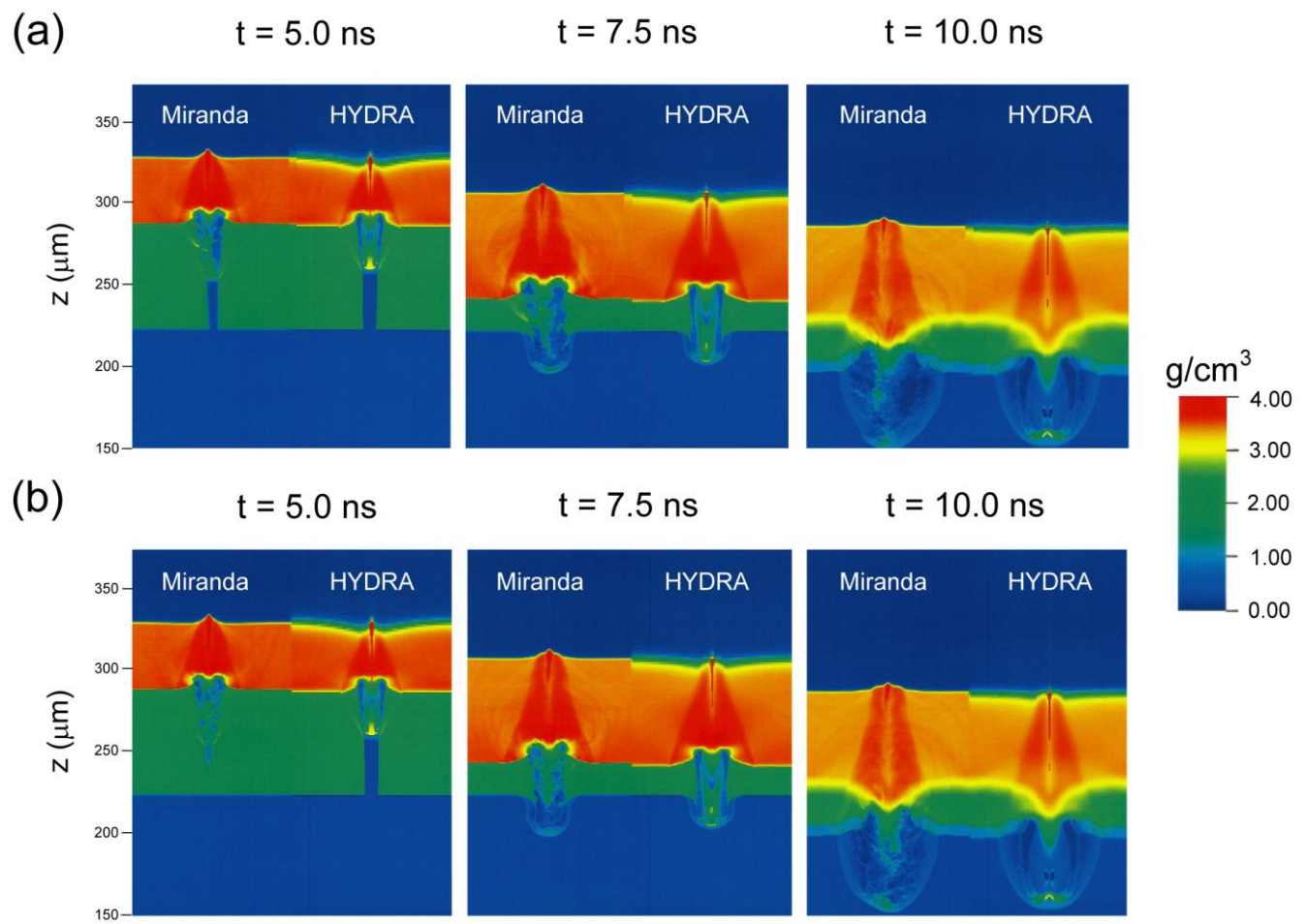


Fig. 18

